

REVIEW ARTICLE

Open Access



Fast and versatile polarization control of X-ray by segmented cross undulator at SPring-8

Jun Miyawaki^{1,2}, Susumu Yamamoto¹, Yasuyuki Hirata¹, Masafumi Horio¹, Yoshihisa Harada¹ and Iwao Matsuda^{1*}

Abstract

An X-ray is the well-known probe to examine structure of materials, including our own bodies. The X-ray beam, especially at the wavelength of nanometers, has also become significant to directly investigate electronic states of a sample. Such an X-ray is called a soft X-ray and polarization dependence of the light-matter interaction further unveils the microscopic properties, such as orbitals or spins of electrons. Generation of high brilliant beams of the polarized X-ray has linked to development of our experimental science, and it has been made by radiation from relativistic electrons at the synchrotron radiation facilities over the world. Recently, we constructed a new polarization-controlled X-ray source, the segmented cross undulator, at SPring-8, the largest synchrotron radiation facility in the world. The operation is based on interference of X-ray beams, which is sharply contrast to the conventional method of regulating electron trajectory by the mechanical control of magnets. The paradigm shift opened the measurement innovations and allowed us to design new experimental approaches to capture signals that have been hidden in materials. The present review describes the novel X-ray source with the principle of operation and the technical details of optimization. Examples of the frontier spectroscopies that use unique optical properties of the source are introduced, followed by the future prospects for next generation synchrotron radiation facilities.

Keywords: X-ray, Synchrotron radiation, Undulator, Spectroscopy

1 Introduction

An X-ray has been a significant experimental probe to investigate creatures in nature. It was named after a ray of “something unknown (X)” by Röntgen but it became widely known by his works [1–3]. Updates of X-ray sources have resulted in the better understanding of samples, and it has led to developments of our science and technology. Today, high-brilliant beams of X-rays are generated by radiation from relativistic electrons by a scheme of Bremsstrahlung (braking radiation) or Synchrotronstrahlung (synchrotron radiation) [4, 5]. Facilities of synchrotron radiation exist all over the world today and are

continuously developed [6], and experimentalists are able to use such X-rays with tunable photon energy. An X-ray has been conventionally classified by ranges of the high photon energy (hard X-ray, 2–10 keV) and the low photon energy (soft X-ray, 0.2–2 keV). The former has been mainly used for structure determination, while the latter for electronic analysis of a sample [7]. Interaction of a matter with a polarized X-ray has found to deepen information of the materials, such as quantum-mechanical characterization of the spin and orbital states [7, 8]. In order to develop material science, a polarization control of synchrotron radiation has been an important issue in the fields of the advanced X-ray optics at a beamline.

A control of the light polarization can now be made by an optical element, i.e., a diamond phase retarder [9], for the hard X-ray region. On the other hand, there is no

*Correspondence: imatsuda@issp.u-tokyo.ac.jp

¹The Institute for Solid State Physics, The University of Tokyo, Kashiwa, Chiba 277-8581, Japan

Full list of author information is available at the end of the article

practical polarizer for the soft X-ray region. Therefore, it is inevitably necessary to control the light polarization by an insertion device (ID) in the electron storage ring. One example is elliptical polarization undulator (EPU), such as an APPLE-type [10, 11]. It controls the polarization by changing the electron trajectory by mechanical arrangements of the magnet arrays that produce the magnetic field [10, 11]. This type of the light source, especially APPLE-II-type, has been widely installed in various synchrotron radiation facilities. The linear and circular polarizations are used for experiments at beamlines.

Cross undulator is another type of ID that generates polarization in a versatile manner. The cross undulator was originally designed by Kim [12], in which IDs with linear horizontal and vertical polarization (LH and LV) are arranged in tandem and the polarization is controlled by the phase between the IDs. If an electromagnet phase shifter (EMPS) is used, it was proposed that the fast polarization switching can be realized at 1 kHz [12], which is much faster than the mechanical change in an APPLE-type undulator that usually takes over minutes. It is worth mentioning that a cross undulator with two IDs of APPLE-II was also proposed by Sasaki et al. [13]. Cross undulators were constructed at facilities of synchrotron radiation and XFEL [14–23]. Polarization control was technically realized but the degree of polarization required much improvement for wide users. The higher degree of polarization can be achieved by a segmented cross undulator (SCU) that was designed by Tanaka et al. [24–26]. Instead of two ID units and one PS in the original cross undulator, more than four units (segments) and three PSs are adopted in the segmented undulator. Despite the promising performance in polarization controls, construction and operation of such a complicated light source has been extremely challenging at a synchrotron radiation facility.

In Japan, we succeeded in developing the world's first SCU as an insertion device, "ID07," at SPring-8 beamline BL07LSU [27–29], shown in Fig. 1, and started the user operation since October 9, 2009. The SCU is composed of eight undulator units and seven PSs. The undulator segment is figure-8 or vertical figure-8 undulator and it is placed alternatively. A figure-8 undulator, Fig. 1(b), generates soft X-ray beam with horizontally linear polarization [30], while a vertical figure-8 one, Fig. 1(c), produce that with vertically linear polarization. It is noted that adoptions of the figure-8 type is to reduce heat loads at the optical axis, which is significant for soft X-ray beamline optics at a high electron energy ring such as SPring-8. The light source ("ID07") can generate various types of the polarizations, such as linear (arbitrary azimuth angle), elliptical, or circular (left- or right-handed) polarization [27]. What is more, we achieved the high-degree of polarization and performed the fast polarization switching using the EMPSs. The light source has become a powerful

probe to investigate material science. The optical character at the beamline is summarized in Table 1 and details of the beamline is described in the reference [27]. To achieve the high optical performance, it has required us to develop the specialized operation procedures.

In the present review article, we record our operations and experiments of the novel and complicated light source of SCU for the coming generations. Followed by the Introduction (Section 1), we describe, the principle, design, and optimization of the light source in Section 2. In Section 3, we introduce examples of experiments with the polarized soft X-rays that are uniquely operated by SCU [31–33]. At last (Section 4), we give future prospects with discussion of the technical improvements of the segmented undulator [34] and the usage in the advanced experiments.

2 The light source

2.1 Principle of radiation from a segmented cross undulator

First, we consider the undulator radiation from an SCU under ideal conditions (no emittance and no energy spread of the electron beam, no error in the magnetic field of the IDs, and only on-axis X-rays are considered) [24, 25]. The simple model of the SCU is shown in Fig. 2. The SCU is composed of M segments of IDs, and each segment has N periods. The odd- and even-number IDs generates horizontally and vertically polarized X-ray, respectively. The total number of segments, M is even number. Phase difference between odd- and even-number (even- and odd-number) IDs is set to φ_1 (φ_2), which is controlled by PS between IDs. The flux, I and the degree of polarization, P_L , P_{L45} , and P_C of the 1st order undulator radiation from this SCU is expressed by the Stokes parameters as [25, 35]

$$I = s_0 = \left(\frac{2\pi M N E_1}{\sqrt{2}\omega_1} \right)^2 S_N S_M \quad (1)$$

$$P_L = s_1/s_0 = 0 \quad (2)$$

$$P_{L45} = s_2/s_0 = \sin(\Psi_1\omega/\omega_1) \quad (3)$$

$$P_C = s_3/s_0 = \cos(\Psi_1\omega/\omega_1) \quad (4)$$

with

$$S_N = \left[\frac{\sin(\pi N((\omega - \omega_1)/\omega_1))}{\pi N((\omega - \omega_1)/\omega_1)} \right]^2 \quad (5)$$

$$S_M = \left[\frac{\sin((M/2)(\Psi_1 + \Psi_2)\omega/\omega_1)}{(M/2) \sin((\Psi_1 + \Psi_2)\omega/\omega_1)} \right]^2 \quad (6)$$

$$\Psi_{1,2} = 2\pi N + \varphi_{1,2} \quad (7)$$

where ω_1 and E_1 are the fundamental energy and the electric field of the 1st order undulator radiation, and ω is the photon energy. E_1 in odd- and even-number IDs are orthogonal, and for ease of discussion, the phase is set to $E_x(\text{odd}) = iE_y(\text{even}) = E_1$ and $E_y(\text{odd}) = E_x(\text{even}) = 0$.



Fig. 1 Photos of the first segmented cross undulator, "ID07," installed at the University-of-Tokyo Outstation Beamline for Materials Science, SPring-8 BL07LSU [27]. **a** A set of the eight ID segments of undulators. **b,c** Arrays of magnets in **b** the horizontal figure-8 undulator segment and **c** the vertical figure-8 undulator segment

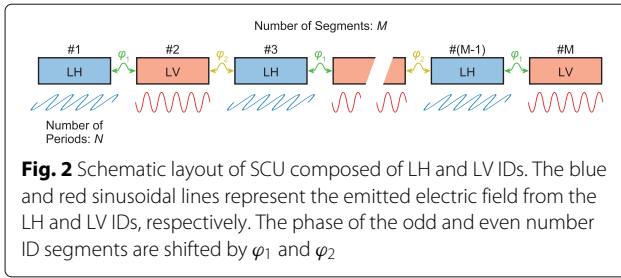
S_N is the spectral profile of the normal undulator radiation, and S_M represents the interference between IDs. Looking at the equation, I , which represents the spectral profile, depends on the phase $\Psi_1 + \Psi_2$, while P_{L45} and P_C depend only on Ψ_1 . This can be understood that Ψ_1

Table 1 Optical parameters at SPring-8 BL07LSU

Photon energy	0.25 ~ 2 keV
Energy resolution	> 10,000
Photon flux	$> 10^{12}$ photons s^{-1} (0.01% bandwidth) $^{-1}$
Polarization control	linear, circular, elliptical
Linear polarization	1.0 (horizontal) 1.0 (vertical)
Circular polarization	0.94 (left-handed) 0.93 (right-handed)
Polarization fast switching	13 Hz

controls the polarization by changing the phase between the LH and LV IDs, while Ψ_2 only adds up the undulator radiation of the same polarization produced by the pairs of the LH and LV IDs and does not affect the polarization. Therefore, when controlling polarization by changing Ψ_1 , by setting Ψ_2 to offset the amount of the change of Ψ_1 and keeping $\Psi_1 + \Psi_2$ constant, we can control only the polarization without changing the flux. Usually, we need the maximum flux at the desired energy, and for this case, $\Psi_1 + \Psi_2 = 2n\pi$.

Figure 3 shows the energy spectra and P_C for $M=4$ and 10 with $\varphi_1 = \varphi_2 = 2\pi$ and $M \times N = 240$. In the SCU, three peaks are obtained due to the interference. In addition to the center peak at ω_1 (hereafter referred to as main peak), two peaks appear on both sides of the main peak at $M=4$ and above (hereafter referred to as side peak). When $M=2$, which is the original cross undulator configuration,



no side peaks appear. This is easily understood by the fact that $S_M=1$ at $M=2$. Looking at P_C , we can see that both main and side peaks have 100% CP. However, the sign of CP is opposite in main and side peaks.

The explanation so far is based on the results calculated under the ideal conditions, but the energy spectra and the degree of polarization are affected (worsened) due to the neglected factors such as emittance and energy spread of the electron beam and the finite acceptance angle of the undulator radiation. In the following, we examine these contributions by considering a specific case of installing an SCU into a long straight section in SPring-8. Ring parameters at the long straight section of SPring-8 is summarized in Table 2. For each segment ID, Figure-8 undulators developed at SPring-8 are employed [30]. ID parameters are summarized in Table 3. Using these parameters, we calculated the undulator radiation of the SCU for different combinations of M and N by the synchrotron radiation calculation code, SPECTRA [36].

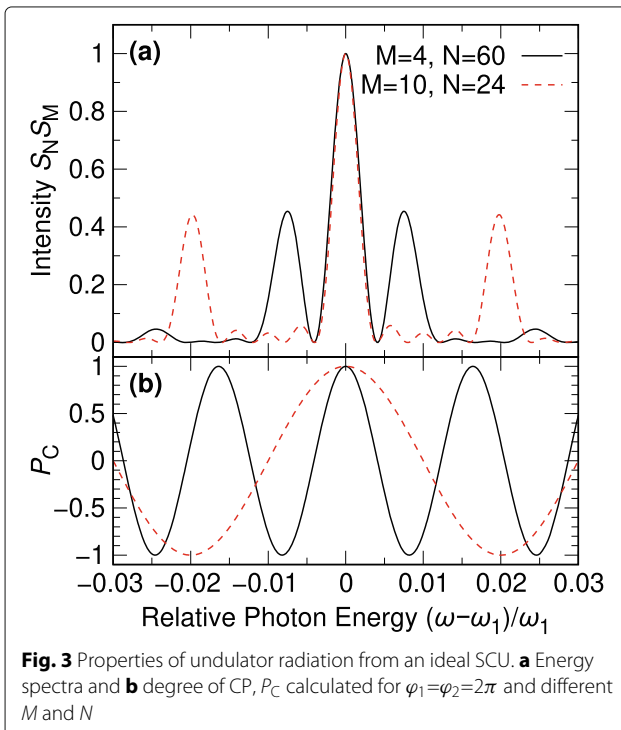


Table 2 Ring parameters at the long straight section of SPring-8

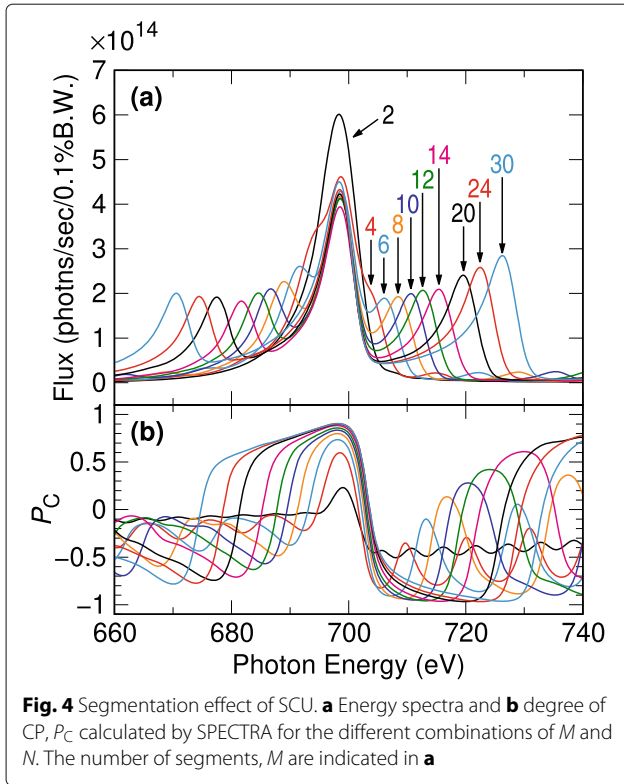
Electron energy	8 GeV
Average current	100 mA
Natural emittance	2.4 nmrad
Coupling	0.002
Energy spread	1.1×10^{-3}
β_x, β_y	34.5 m, 9.7 m
η_x, η_y	0.153 m, 0 m

A drift space, which is the space between IDs, was set to 0.5 m. The acceptance was set to twice the effective divergence, σ'_p for both horizontal and vertical directions, instead of a constant acceptance size, because the σ'_p varies with the number of segments, M . σ'_p is the convolution of the natural divergence and the divergence of the electron beam, $\sqrt{\sigma_r'^2 + \sigma^2}$. The phase φ_1 was set to 0.5π to create CP, and φ_2 was set to 1.5π to maximize the flux.

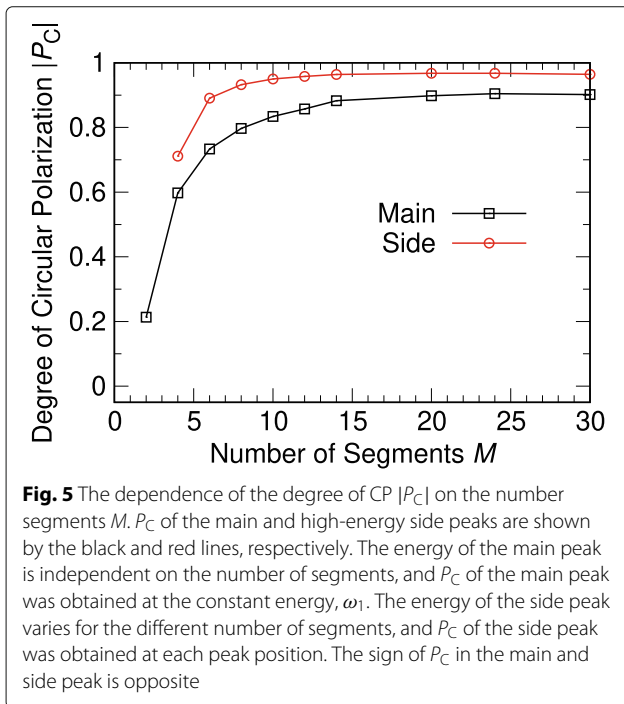
Figure 4 shows the calculated energy spectra and the degree of CP, P_C for different M and N . The main and side peaks appear as in the ideal case. However, in the realistic calculations, P_C is not 1.0, and P_C of the main and lower-energy side peaks deteriorates due to the tail of higher-energy peak toward lower energy. In particular, the effect of the tail of the main peak on the side peak on the low-energy side is significant. On the other hand, the side peak on the high-energy side is not affected by the tail and thus has even higher degree of CP than that of the main peak. For more quantitative discussion, P_C of the main peak and the side peak on the high-energy side are shown in Fig. 5. P_C of the high-energy side peak is obviously higher than that of the main peak. When the number of segments is set to 2 (the case of the original cross undulator), only the main peak appears as mentioned earlier, and P_C is ~ 0.2 , which makes it completely useless in terms of the degree of the polarization. P_C of the main peak saturates at ~ 0.9 , while P_C of the side peak is >0.9 for more than 8 segments, and >0.95 for more than 12 segments. From these results, when the higher degree of the polarization is required, it is better to use the side peak on the

Table 3 ID parameters for the calculations

Type	Horizontal and vertical figure-8
Periodic length, λ_u	10 cm
$M \times N$	~ 240
M	2, 4, 6, 8, 10, 12, 14, 20, 24, 30
N	120, 60, 40, 30, 24, 20, 16, 12, 10, 8
$K_x(y), K_y(x)$	
for horizontal (vertical) figure-8 undulator	1.93, 3.41
$\hbar\omega_1$	700 eV



high-energy side. The number of segments will be determined by considering the decrease in brilliance due to the drift space and the increase in P_C due to larger number of segments. In this case, 8, 10, or 12 segments would be reasonable.

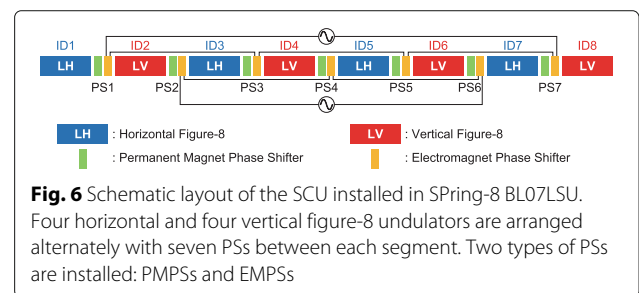


Thus, in a real system, the original cross undulator is useless due to the factors such as the emittance and energy spread of the electron beam and finite acceptance angle. This is because the ID pair is too long for undulator radiation from the two IDs to interfere with each other. The SCU, on the other hand, can set the length of each ID pair less than the interference distance, thus improving P_C . The interference distance can be understood as follows. Considering that the interference determines the monochromatic nature of the undulator radiation as $\frac{\sigma_\omega}{\omega} \approx \frac{1}{2N}$, we can define the effective number of periods, N_{eff} , from the actual monochromatic nature, $\frac{\sigma_\omega}{\omega} = \frac{1}{2N_{\text{eff}}}$, and obtain the effective interference distance, $L_{\text{eff}} = N_{\text{eff}} \times \lambda_u$. Here, σ_ω is the standard deviation of the peak at ω in the energy spectra. In the present case, $N_{\text{eff}} \approx 100$, and then $L_{\text{eff}} \approx 10$ m. In the case of $M = 4$ and $N = 60$, the length of the ID pair is 12.5 m, which is longer than the effective interference distance (10 m), and P_C is 0.71. In the case of $M = 6$ and $N = 40$, the length of the ID pair is 8.5 m, which is shorter than the effective interference distance, and thus P_C is improved to 0.9. The concept of the effective interference distance can reasonably explain the result of the calculation and would be a good guideline for designing an SCU.

We have explained the principle of the segmented undulator for the case of the SCU, where circularly polarized X-ray is generated by two different linearly polarized X-ray, but it should be noted that the same principle can be applied to the case where linearly polarized X-ray is generated by two helical undulators with the opposite helicity. In addition, although we have shown a specific example of SCU for soft X-rays, it is not limited by the energy region as shown in 2.1, and does not preclude its application to the hard X-ray region. However, as shown in [25], the effect of the emittance is relatively larger in hard X-rays, so the emittance required to achieve the same level of performance becomes smaller.

2.2 Design of "ID07" in Spring-8

Schematic layout of "ID07" is shown in Fig. 6. "ID07" is an SCU consisting of four horizontal and four vertical figure-8 undulators arranged alternately in a long straight section of SPring-8 and can generate LH, LV, and CP



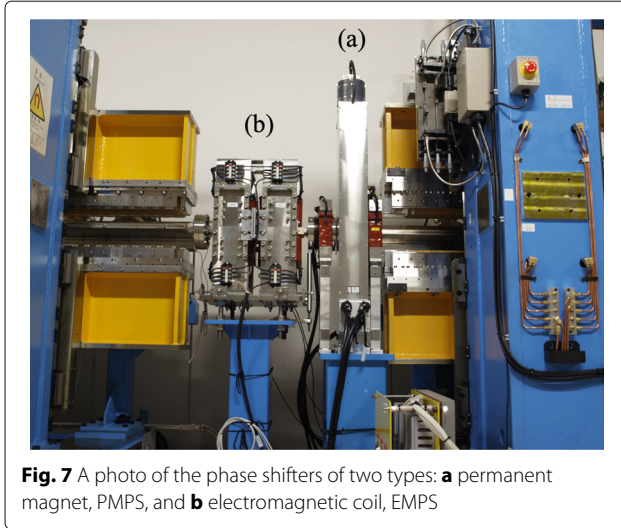


Fig. 7 A photo of the phase shifters of two types: **a** permanent magnet, PMPS, and **b** electromagnetic coil, EMPS

(elliptical polarization) by controlling the phase with permanent magnet and electromagnet PSs (PMPSs and EMPSs) placed between IDs [27, 29], as shown in Fig. 7. Eight segmentations were employed considering the brilliance and the degree of the polarization. The parameters of the horizontal and vertical figure-8 undulators are summarized in Table 4. The numbers of periods are different between the horizontal and vertical figure-8 undulators, because the length of the vertical figure-8 undulator was reduced to install special octupole magnets after the installation of the horizontal figure-8 IDs to keep the injection efficiency. Two different types of PSs, PMPSs, and EMPSs are installed in all the seven drift spaces. The periodic length and the number of the periods for the PMPSs are 100 mm and 1, respectively. The seven PMPSs can set the path length independently. The EMPSs, on the other hand, are designed to be used together with the PMPSs: first, the PMPSs are used for the static phase matching, and the EMPSs are used only for fast polarization switch. As explained in the previous section, the

Table 4 ID parameters of horizontal and vertical figure-8 undulators comprising the SCU installed in SPring-8 BL07LSU

	Horizontal figure-8	Vertical figure-8
Device length (m)	2.6	2.0
Periodic length (mm)	100	100
Number of regular periods	24	18
Regular magnet length (m)	2.4	1.8
Minimum gap (mm)	28	20
Maximum gap (mm)	150	150
Peak magnetic fields, B_x (T)	0.12	0.68
Peak magnetic fields, B_y (T)	0.71	0.15

phases at PS1, PS3, PS5, and PS7 are modulated in the same way, and the phases at PS2, PS4, and PS6 are modulated to cancel the phase modulation by PS1, PS3, and PS5. Therefore, the EMPSs are divided into two groups (odd- and even-number EMPSs) and controlled by two power supplies.

In the normal operation of “ID07,” the following three modes are used to generate LH, LV, and CP. In LH (LV) mode, ID1, ID3, ID5, and ID7 (ID2, ID4, ID6, and ID8) are used, and in CP mode, all eight IDs are used. In LH and LV modes, because the polarization of each ID is the same, the phase between each ID only changes the flux but not the polarization. In contrast, in CP mode, because the LH and LV IDs are used, the degree of CP changes depending on the phase between the LH and LV IDs. The energy spectra and the degree of the polarization was calculated by SPECTRA [36] at $\hbar\omega_1=700$ eV in CP mode using eight IDs with different phase between the LH and LV IDs. Figure 8 shows the calculated energy spectra and the degree of the polarization. When the phase at the odd-number PSs, φ_1 was changed, the sum of the phases φ_1 and φ_2 at the odd- and even-number PSs was kept 2π . Consequently, the energy spectra are the same for any φ_1 . The best degree of CP is 0.94 at $\varphi_1=0.5\pi$, while at $\varphi_1=0.4\pi$ and $\varphi_1=0.3\pi$, the degree of CP significantly decreases to 0.88 and 0.74, respectively. Because the energy spectra do not

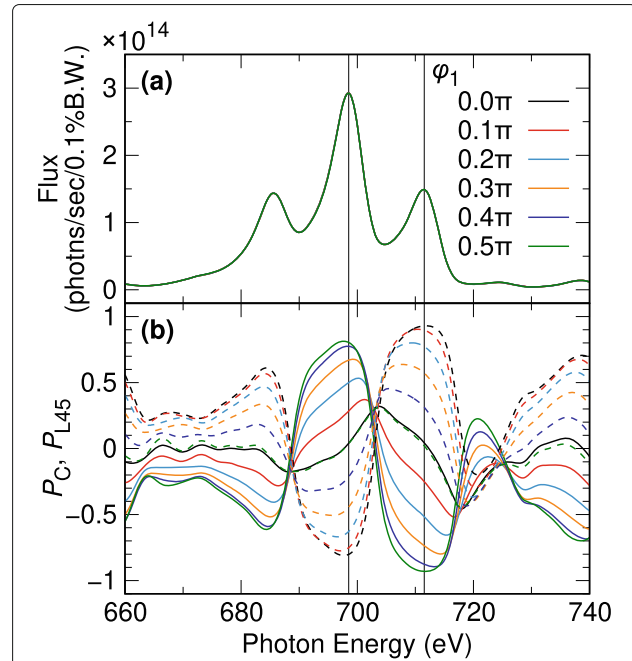


Fig. 8 Spectra of “ID07.” Calculated **a** energy spectra and **b** degree of polarization for “ID07” at $\hbar\omega_1=700$ eV in CP mode using eight IDs. φ_1 is the phase at the odd-number PSs. The sum of the phases φ_1 and φ_2 at the odd- and even-number PSs is 2π . Solid and dashed lines are P_C and P_{L45}

change with the polarization, it is essential to adjust φ_1 by measuring the degree of the polarization. What is worse in the real operation, if φ_1 is not adjusted properly, the polarization of each pair becomes different, resulting in more chaotic situation. Thus, the precise phase control is very important to obtain the high degree of the polarization.

2.3 Precise phase optimization

The precise control of the phase is crucial to obtain high flux all over the energy range with high degree of the polarization. In this section, we will explain how to optimize the phase in “ID07” to maximize the flux and the degree of polarization by the PMPSs and how to realize fast polarization switch by EMPSSs.

2.3.1 Static phase control by permanent magnet phase shifters

In “ID07,” the phase shift between each ID is optimized by maximizing the flux in LH and LV modes, while the phase shift is optimized by measuring the degree of the polarization in CP mode. The conditions of the phase matching in LH, LV, and CP modes are

$$p(g) + \Delta_{h,v}(\lambda) = (n_{h,v} + 1/2)\lambda \quad (8)$$

LH and LV modes:

$$p(g) + \Delta_c(\lambda) = (n_c \pm 1/4)\lambda \quad (9)$$

CP mode:

where $p(g)$ is a path length induced by PS, g is the gap of PMPS, $\Delta(\lambda)$ is a path length independent of the gap of PMPS, such as the path length at a drift section and the effect of the end magnetic field of ID, λ is the fundamental wavelength of ID, and n is an integer. The addition of $1/2$ in LH and LV modes is due to the fact that the magnetic field polarities of adjacent IDs with the same polarization (e.g., ID1 and ID3) are inverted with respect to each other.

The phase at PS is optimized based on these conditions. In LH and LV modes, the phase only changes the flux and has no effect on the polarization because only IDs with the same polarization are used. Therefore, the phase difference can be investigated by measuring the flux, and the gap of PS can be easily and experimentally determined in the whole energy range. On the other hand, to determine the gap of PS in CP mode, it is necessary to measure the degree of the polarization by some method such as polarization analysis or X-ray magnetic circular dichroism (XMCD). However, the polarization analysis and XMCD require a polarizer and a sample which shows the XMCD signal for each desired energy, respectively, and hence, it is impractical to determine the gap of PS in CP mode at many energies in the entire energy range. Therefore, it is required to analytically determine the gap of PS for CP mode using the results of the PS optimization for LH and LV modes.

As an example of the PS optimization in LH mode, the variation of the flux as a function of the PS gap is shown in Fig. 9. The gaps of ID1 and ID3 were set to $\hbar\omega=980$ eV, and the gap of PS1 was scanned. Since ID1 and ID3 are both LH IDs, the flux is maximized when the phase is matched, and the variation of the flux shows a sinusoidal intensity modulation. Thus, there are multiple PS gaps satisfying the phase matching equation at a given energy. By performing similar measurements in the $\hbar\omega$ range of 250–2000 eV with other pairs of IDs, we obtain many sets of g and λ satisfying the phase matching equation for all seven PSs. The result of the PS1 optimization for a pair of ID1 and ID3 is shown in Table 5. From these sets of g and λ , $p(g)$, $\Delta_{h,v}(\lambda)$, and $n_{h,v}$ has to be determined. Since $p(g)$ was estimated from the measurement of the magnetic field in PMPS, $p(g)$ was first determined.

When the optimal gaps for a given wavelength, λ_i are g_{i1} , $g_{i2}, \dots, g_{ij}, \dots$, the phase matching equations are

$$p(g_{i1}) + \Delta(\lambda_i) = (n_i + 1/2)\lambda_i \quad (10)$$

$$p(g_{i2}) + \Delta(\lambda_i) = ((n_i + 1) + 1/2)\lambda_i \quad (11)$$

\vdots

and can be transformed to

$$p(g_{i(j+1)}) - p(g_{ij}) = \lambda_i. \quad (12)$$

Introducing the amount of the phase shift, $P_\lambda(g) = 2\pi \frac{p(g)}{\lambda}$, we have

$$P_{\lambda_i}(g_{i(j+1)}) - P_{\lambda_i}(g_{ij}) = 2\pi. \quad (13)$$

As expected, the phase difference at neighboring g that gives the maximum flux at a given photon energy is 2π , regardless of the energy. The pairs of g_{ij} and $g_{i(j+1)}$ taken from the results in Table 5 are shown in Table 6. We approximated $p(g) = \exp(K_0 + K_1g + K_2g^2)$ and optimized K_0, K_1, K_2 to satisfy $P_{\lambda_i}(g_{i(j+1)}) - P_{\lambda_i}(g_{ij}) = 2\pi$

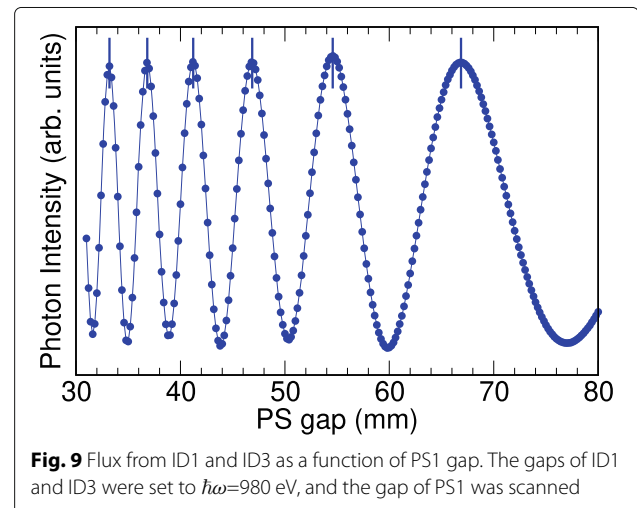


Fig. 9 Flux from ID1 and ID3 as a function of PS1 gap. The gaps of ID1 and ID3 were set to $\hbar\omega=980$ eV, and the gap of PS1 was scanned

Table 5 Optimal gaps of PS1 at each energy determined by maximizing the flux from ID1 and ID3

Energy (eV)	g_{i1} (mm)	g_{i2} (mm)	g_{i3} (mm)	g_{i4} (mm)	g_{i5} (mm)	g_{i6} (mm)	g_{i7} (mm)	g_{i8} (mm)	g_{i9} (mm)	g_{i10} (mm)	g_{i11} (mm)	g_{i12} (mm)	g_{i13} (mm)
250	63.500	36.314											
275	43.791												
300	53.599	35.408											
325	65.929	40.881											
355	49.711	35.519											
390	62.093	42.048	32.086										
420	49.396	37.001											
460	62.311	44.218	34.691										
500	52.346	40.241	32.649										
545	65.501	47.628	38.114	31.689									
570	79.786	53.694	42.165	34.806									
610	64.659	48.607	39.568	33.350									
665	59.481	46.854	39.012	33.372									
715	76.870	55.761	45.297	38.389	33.220								
760	66.038	51.676	43.153	37.157	32.532								
820	62.295	50.365	42.790	37.250	32.923								
870	78.400	59.261	49.036	42.225	37.080	33.013							
930	74.551	58.082	48.815	42.431	37.549	33.629							
980	66.851	54.572	46.863	41.216	36.817	33.186							
1035	63.115	52.821	45.969	40.790	36.668	33.253							
1095	77.758	61.502	52.260	45.859	40.976	37.016	33.725						
1140	69.811	57.646	49.988	44.340	39.939	36.290	33.225						
1195	66.453	56.060	49.145	43.928	39.771	36.316	33.368						
1255	64.784	55.442	48.939	44.017	40.007	36.677	33.807	31.320					
1310	74.950	61.855	53.823	47.953	43.403	39.668	36.509	33.779	31.384				
1360	70.063	59.375	52.286	46.983	42.747	39.255	36.244	33.655	31.351				
1410	66.347	57.347	50.985	46.142	42.184	38.888	36.031	33.545	31.337				
1460	75.268	63.098	55.385	49.703	45.241	41.573	38.452	35.760	33.373	31.260			
1510	71.035	60.893	53.989	48.810	44.628	41.177	38.197	35.621	33.347	31.282			
1565	68.484	59.539	53.184	48.334	44.379	41.064	38.211	35.706	33.514	31.493			
1620	77.587	65.462	57.667	51.991	47.490	43.813	40.672	37.968	35.564	33.450	31.519		
1675	74.988	64.238	56.986	51.643	47.336	43.798	40.755	38.118	35.776	33.690	31.804		
1725	70.014	61.247	55.005	50.185	46.267	42.960	40.133	37.620	35.411	33.405	31.603		
1780	79.938	67.854	59.953	54.214	49.672	45.961	42.778	40.064	37.629	35.487	33.531	31.775	
1835	76.053	65.706	58.595	53.320	49.065	45.548	42.522	39.900	37.569	35.479	33.593	31.873	
1895	73.791	64.476	57.898	52.908	48.861	45.456	42.553	39.993	37.729	35.677	33.840	32.138	
1950	71.464	63.052	57.040	52.317	48.490	45.231	42.429	39.949	37.744	35.753	33.952	32.299	
2000	79.123	68.314	61.004	55.614	51.274	47.680	44.623	41.951	39.593	37.465	35.560	33.804	32.209

Table 6 Pairs of PS1 gaps giving phase difference of 2π at a given energy obtained from the PS optimization with ID1 and ID3

Index	Energy (eV)	g_i (mm)	$g_{i(j+1)}$ (mm)
0	250	36.314	63.500
1	300	35.408	53.599
2	325	40.881	65.929
3	355	35.519	49.711
4	390	32.086	42.048
5	390	42.048	62.093
6	420	37.001	49.396
7	460	34.691	44.218
8	460	44.218	62.311
9	500	32.649	40.241
10	500	40.241	52.346
11	545	31.689	38.114
12	545	38.114	47.628
13	545	47.628	65.501
14	570	34.806	42.165
15	570	42.165	53.694
16	570	53.694	79.786
17	610	33.350	39.568
18	610	39.568	48.607
19	610	48.607	64.659
:	:	:	:

at all the pairs for seven PSs. The optimized $p(g)$ for at seven PSs is shown in Fig. 10. Although the values of the optimized $p(g)$ are slightly larger than that estimated from the measurements of the magnetic field in PS, the optimized $p(g)$ are in good agreement among the seven PSs.

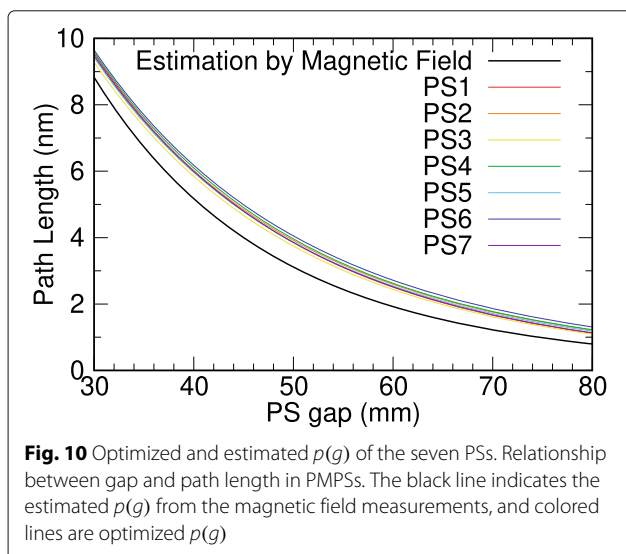
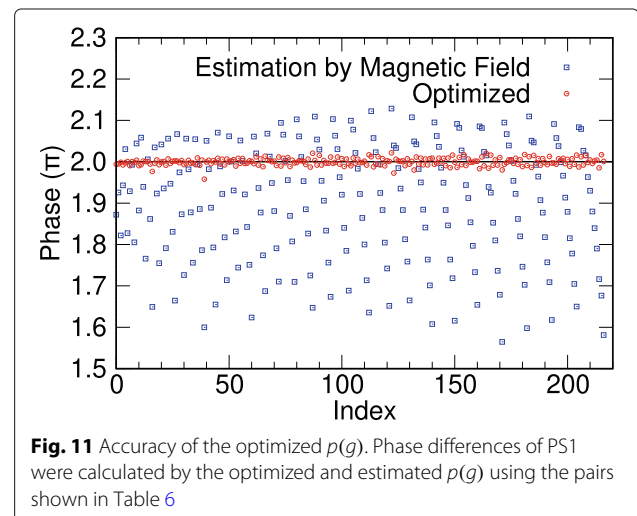
**Fig. 10** Optimized and estimated $p(g)$ of the seven PSs. Relationship between gap and path length in PMPs. The black line indicates the estimated $p(g)$ from the magnetic field measurements, and colored lines are optimized $p(g)$

Figure 11 shows the phase difference, $P_{\lambda_i}(g_{i(j+1)}) - P_{\lambda_i}(g_{ij})$ for the pairs in Table 6 calculated from the optimized and estimated $p(g)$. Although the phase differences calculated from the estimated $p(g)$ deviates significantly from 2π , the phase difference calculated from the optimized $p(g)$ are $2 \pm 0.02\pi$ for all pairs. Thus, it was confirmed that $p(g)$ was successfully optimized, and the path length of PS is determined only by the gap of PS and not affected by the ID gaps.

The path lengths for λ and g obtained from the PS1 and PS6 optimization in the LH and LV modes were calculated by the optimized $p(g)$ and are shown as circles in Fig. 12. λ and g obtained from the PS1 optimization was summarized in Table 5. From the phase matching Equation (10), $p(g) = (n + 1/2)\lambda - \Delta(\lambda)$, and the dependence of $\Delta(\lambda)$ on λ is expected to be small, linear relationship with slope of $\sim (n + 1/2)$ and intercept of $\sim \Delta$ should be found for a certain n . Accordingly, a set of path lengths for the same n was estimated and fitted with a line (straight lines in Fig. 12). The linear fitting is very good, suggesting that $\Delta(\lambda)$ is constant or linear. The slope obtained from the fitting is shown in Fig. 13. In LH mode, the slope is almost equal to $n + 1/2$, while in LV mode, the slope is slightly different from $n + 1/2$. When $n=4$ ($n=5$) was set to the smallest integer in the LH (LV) mode, all the points were connected with best-physically reasonable $\Delta(\lambda)$. Thus, n was determined for both LH and LV mode. Using these n , $\Delta(\lambda) = (n + 1/2)\lambda - p(g)$ was calculated and are shown in Fig. 14. As expected from the fitting results, $\Delta_h(\lambda)$ is constant, while $\Delta_v(\lambda)$ becomes longer at longer wavelength, which can be understood that the influence of the magnet field at the end of the vertical figure-8 ID is not negligible at the small gap.

From the PS optimization in the LH and LV, $p(g)$ was optimized, and $\Delta_h(\lambda)$ was found to be constant, while $\Delta_h(\lambda)$ had approximately-linear relationship with

**Fig. 11** Accuracy of the optimized $p(g)$. Phase differences of PS1 were calculated by the optimized and estimated $p(g)$ using the pairs shown in Table 6

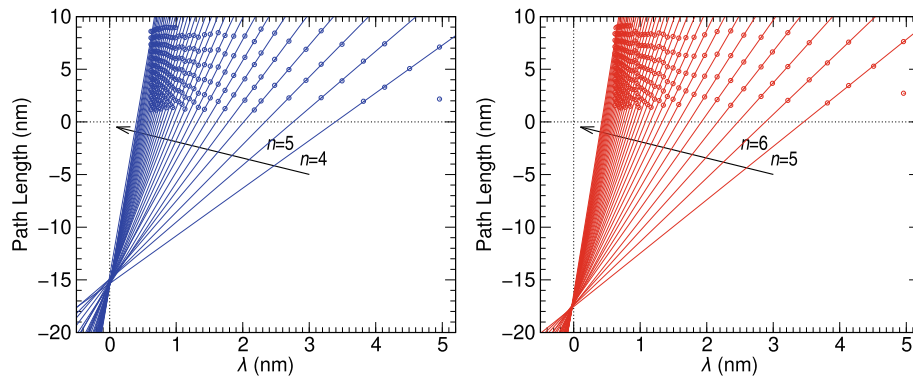


Fig. 12 Path length at the optimal gaps as a function of λ . The path length of PS1 (left) and PS6 (right) in LH and LV mode, respectively, are shown. Calculated values from the optimal gaps are shown in circles. Solid lines are the results of linear fitting

λ . From these results, we determine $\Delta_c(\lambda)$ and n_c in CP mode. In the PS optimization for CP mode, the PS gaps were optimized from polarization and flux measurements at four energies: 298, 398, 708.2, and 740 eV. In the PS optimization for CP mode, PS1 (PS3, PS5, PS7) between ID1 and ID2 (ID3 and ID4, ID5 and ID6, ID7 and ID8) were first optimized by measuring the degree of the polarization. Next, PS2 (PS6) between ID1-PS1-ID2 and ID3-PS3-ID4 (ID5-PS5-ID6 and ID7-PS7-ID8) were optimized by measuring the flux. Finally, PS4 between ID1-PS1-ID2-PS2-ID3-PS3-ID4 and ID5-PS5-ID6-PS6-ID7-PS7-ID8 was optimized by measuring the flux. As mentioned before, among the three peaks appear-

ing in the energy spectra, the degree of CP is the highest at the high-energy side peak [27]. Therefore, we first optimized the CP for the main peak to find out the energy position of the side peak. Then, the main energy was set so that the side peak appears at the desired energy, and the gap of PSs were optimized in the same way.

Figure 15 shows the path length when the gap of PS1 was set to obtain CP from ID1 and ID2. By the same analysis as for LH and LV mode, n_c was determined. As shown in Fig. 15(a), $n_c = 2$ was estimated to be the smallest integer. Δ_c for the seven PSs obtained from this n_c is shown in Fig. 15(b). Δ_c for the even-number PSs is smaller than that for the odd-number PS. Since the vertical figure-8 undulators are shorter than the horizontal figure-8 undulators, the length of the drift section at the even-number PS is shorter than that at the even-number PS, and Δ_c is smaller for the even-number PS. Based on the results of the PS optimization for LH and LV modes, $\Delta_c(\lambda)$ was determined by linear fitting, assuming that $\Delta_c(\lambda)$ also had a linear dependence on λ .

From the analysis of the PS gap optimization for CP mode, n_c and $\Delta_c(\lambda)$ have been determined, and the ID and PS gaps for CP mode in the entire energy range can be analytically determined. In CP mode, the fundamental energy of ID has to be offset to use the high-energy side peak in the energy spectrum of ID to obtain high degree of CP. The energy position of the side peak at a given energy can be found from Fig. 2 to be $(\omega - \omega_1)/\omega_1 = 1/(2N + \varphi_1/\pi)$. In the case of "ID07," $(\omega - \omega_1)/\omega_1 = 1/(2(N + n_c) + 1/2)$, and it should be noted that the energy position of the side peak slightly changes depending on n_c . However, when $n_c \ll N$, the change in the energy position due to the difference in n_c is negligible, also considering the spectral width. While the parameters for the ID gap are prepared taking this into account, the analytically determined parameters for the PS gap allow the use of CP mode in the entire energy range.

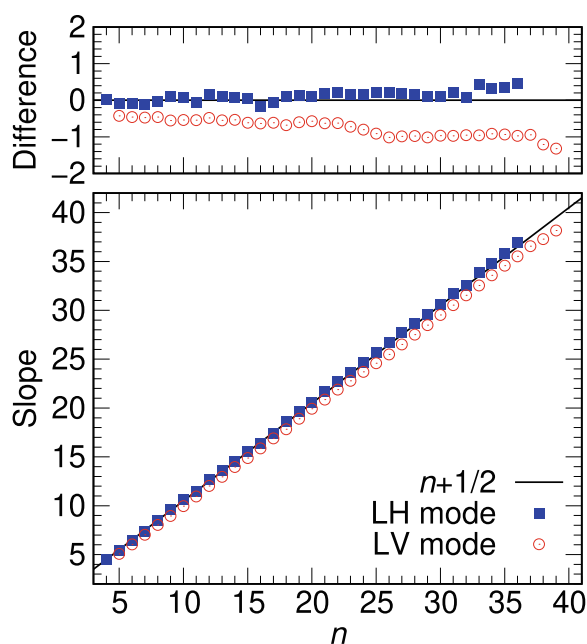
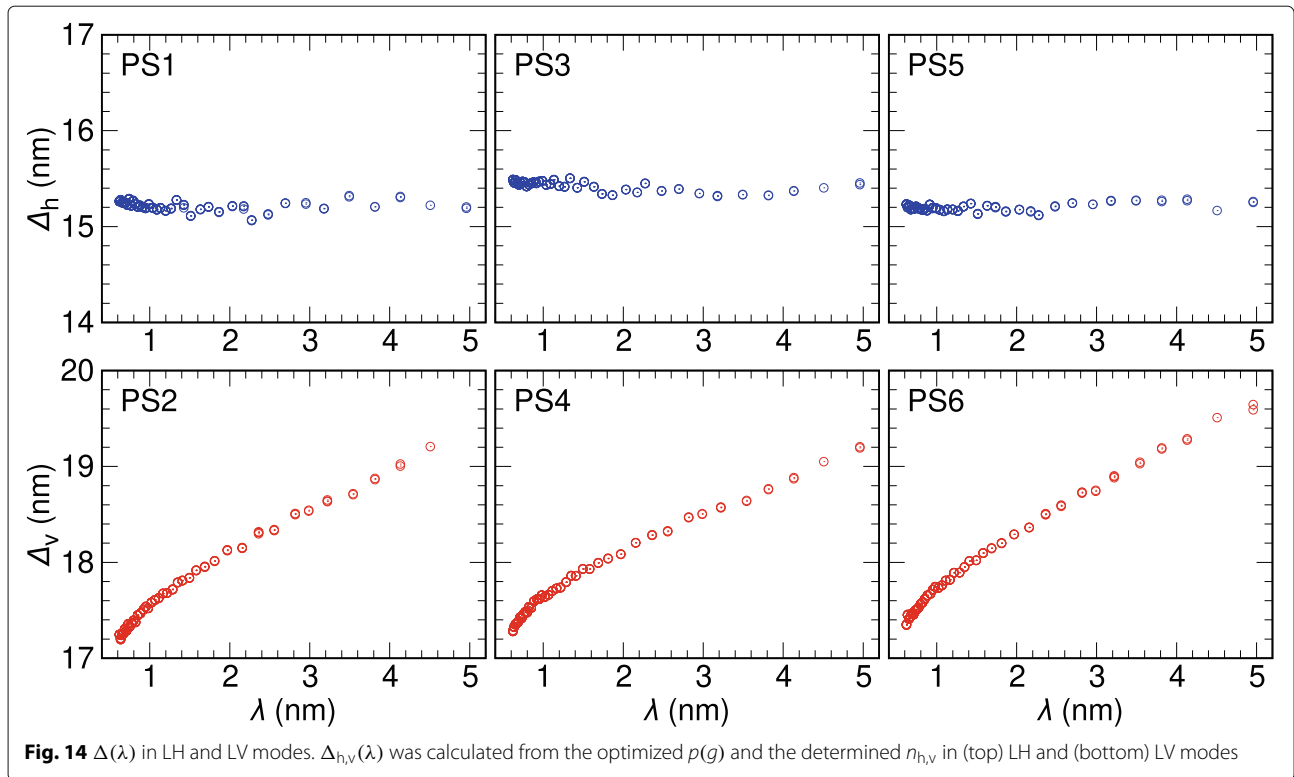
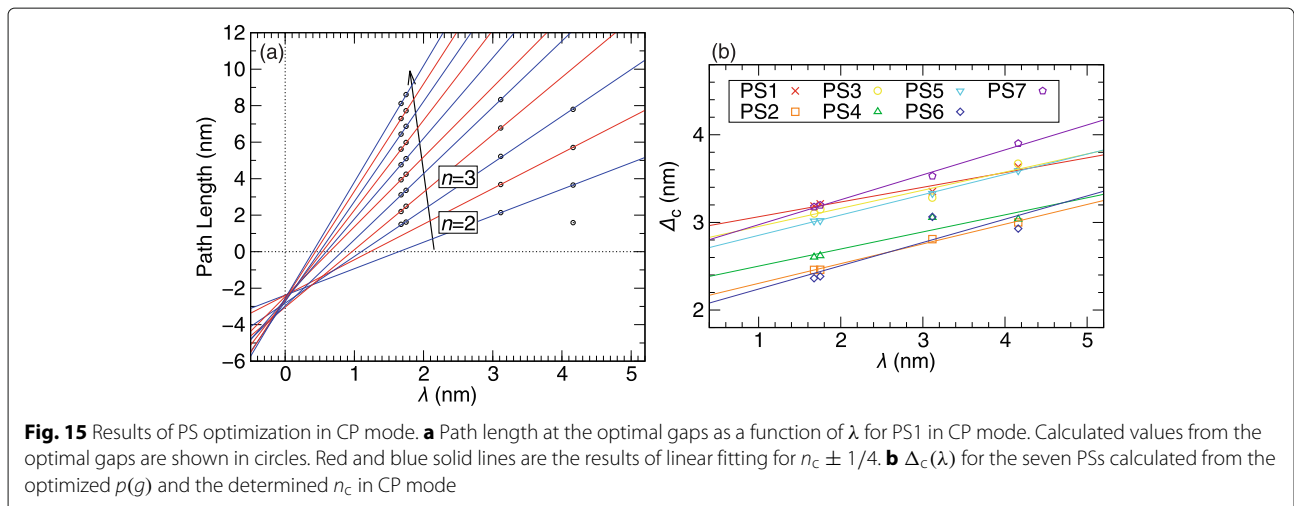


Fig. 13 Slope parameters in the LH and LV modes. (bottom) Slope of linear fitting of path length vs λ plot and (top) difference of slope from $n + 1/2$. Squares and circles are the results of the linear fitting, and the black solid line is $n + 1/2$



In order to confirm the validity of the obtained ID and PS gaps for CP mode, we measured the energy dependence of the photon flux. In CP mode, the flux does not give us any direct information about the degree of the polarization, but by confirming the smooth variation of the flux with the photon energy, we can evaluate whether the phase is in the aforementioned chaotic situation or not. Since we have confirmed that the degree of the polarization at the four energies used for the PS optimization is comparable to the design value, we can conclude that

the ID and PS gap parameters are reasonable if the flux curve does not show unnatural intensity changes at the energies in between the four energies. The measured photon flux in CP mode is shown in Fig. 16. For comparison, the flux in LH mode is also shown. The photon flux in CP mode also shows the smooth intensity change as in LH mode. In particular, the photon flux in CP mode does not show any unnatural intensity changes at energies other than those four energies. The ID energy spectra in CP mode are shown in Fig. 17. The energies of the side peaks



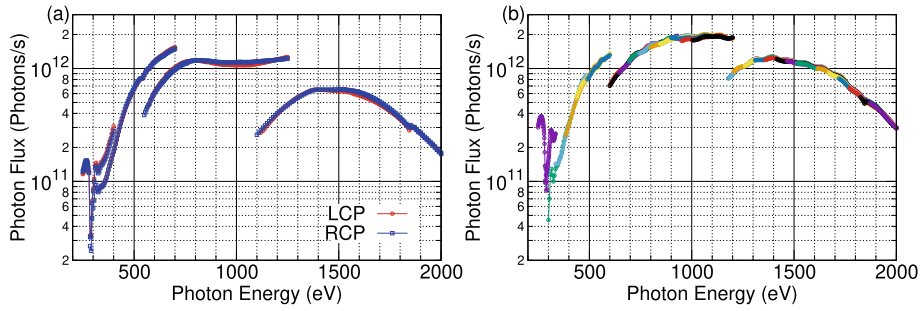


Fig. 16 Photon flux of BL07LSU in CP and LH modes. **a** Photon flux in CP mode. The red and blue circles correspond to the photon flux of left and right CP (LCP and RCP) modes, respectively. **b** Photon flux in LH mode. Different colors indicate different n

match the desired energies even for the different n in the result of $\hbar\omega=708.2$ eV, indicating that the ID gap has been properly determined. Thus, we concluded that the ID and PS gap parameters for CP mode were well determined by the analytical method.

2.4 Rotation of linear polarization

The SCU at BL07LSU of SPring-8 [27] consists of eight ID segments and seven PSs as depicted in Fig. 18(a). Horizontal and vertical polarization can be produced by selectively activating corresponding IDs that are positioned alternately (Figs. 18(b) and (c)). In order to produce linear polarization at a demanded azimuthal angle, we superimpose a set of circularly polarized light with opposite helicity. In this operation mode, the front four IDs [Set A] are designated to yield right (left) circular polarization and the rear four IDs [Set B] to left (right) circular polariza-

tion. A relative phase difference is controlled by the PS in between [PS4 in Fig. 18(d)].

The principle of polarization-angle rotation can be readily understood from the following consideration. The electric field vector of left and right circularly polarized light, E_L and E_R , are expressed as follows:

$$E_L = \begin{pmatrix} \cos \omega t \\ \sin \omega t \end{pmatrix}, E_R = \begin{pmatrix} \sin \omega t \\ \cos \omega t \end{pmatrix}. \quad (14)$$

When each circular polarization is superimposed with a relative phase shift of 2θ , resulting electric field is given by

$$E = \begin{pmatrix} \cos \omega t \\ \sin \omega t \end{pmatrix} + \begin{pmatrix} \sin(\omega t - 2\theta) \\ \cos(\omega t - 2\theta) \end{pmatrix} \\ = \begin{pmatrix} 2 \cos(\theta + \pi/4) \sin(\omega t - \theta + \pi/4) \\ 2 \sin(\theta + \pi/4) \sin(\omega t - \theta + \pi/4) \end{pmatrix}. \quad (15)$$

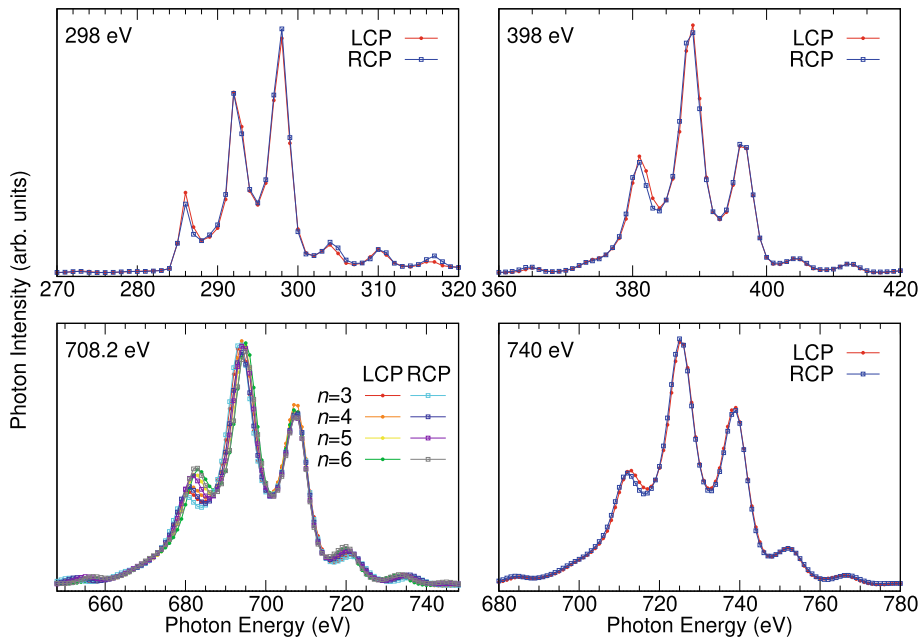
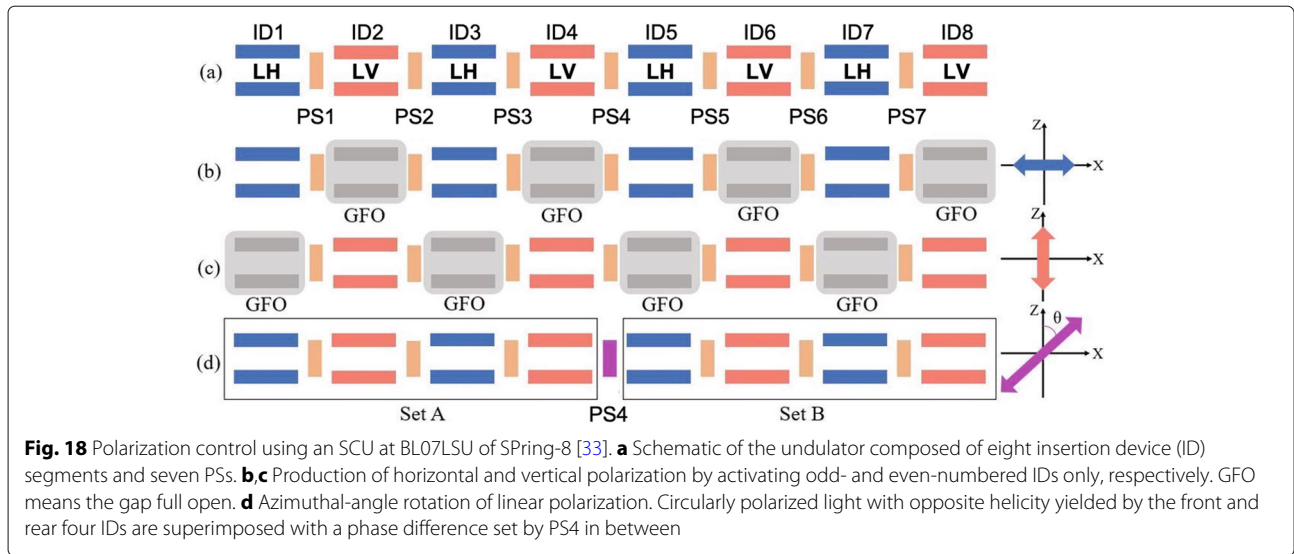


Fig. 17 Energy spectra in CP mode for different energies. At $\hbar\omega=708.2$ eV, energy spectra for different n_c are also shown



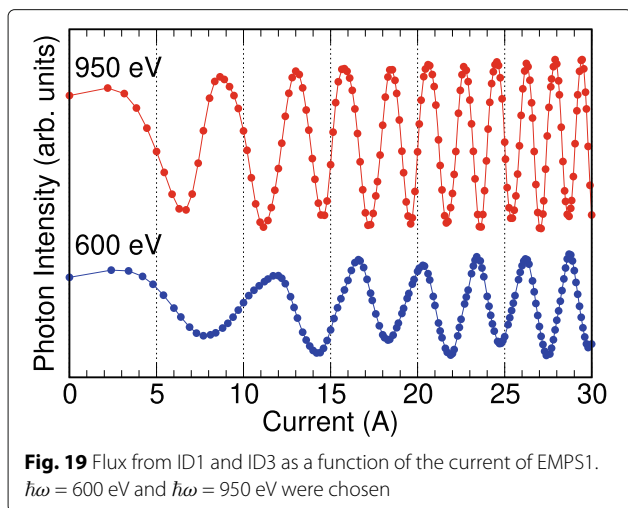
The ratio between x and y components,

$$E_y/E_x = \tan(\theta + \pi/4), \tag{16}$$

is independent of time, indicating that outgoing light is linearly polarized but rotated by $\theta + \pi/4$ from the horizontal direction. The rotation angle θ is solely determined by the relative phase shift, which is controllable in a continuous fashion. Thus, the present SCU can deliver linearly polarized light at any azimuthal angles on demand from experiments.

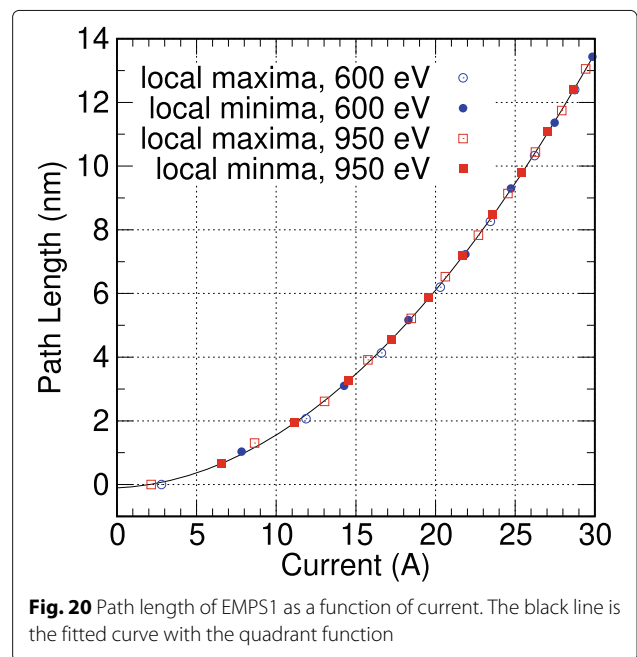
2.5 Dynamic phase control by electromagnet phase shifters

First, we calibrated the relationship between the current and the phase shift of EMPS. In LH mode, the gap of PMPS1, i.e., PS1 with PM, was first optimized by the flux measurement for the pair of ID1 and ID3, and then the flux was measured by varying the current of EM at PS1,



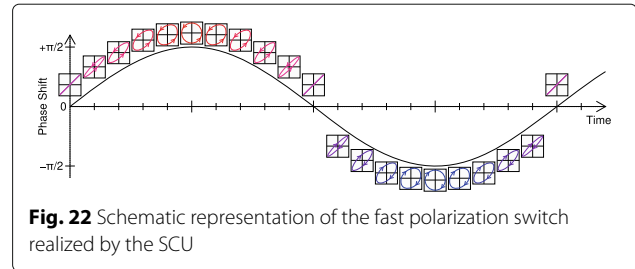
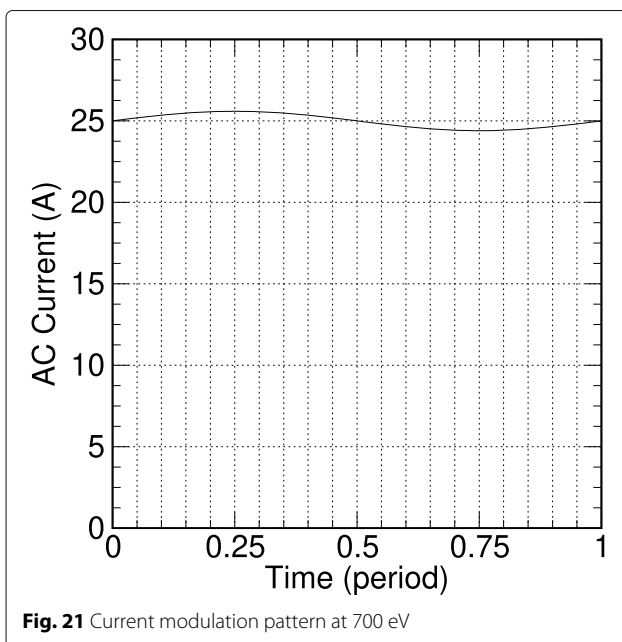
i.e., EMPS1 (Fig. 19). $\hbar\omega=600$ eV and $\hbar\omega=950$ eV were chosen. The path length was calculated assuming that the phases at local maxima and minima are $2n\pi$ and $(2n+1)\pi$, respectively (Fig. 20). The fitting with a quadratic function was very good, and we obtained a calibration curve of the EMPS. Since the phase shift in the EMPS is proportional to the square of the current, the required current modulation becomes smaller if the current is modulated at a higher current. Therefore, for the fast polarization switch, the current is modulated around 25 A in “ID07.”

For the fast polarization switch, how to set the gap of PMPSs and EMPSs is explained below. In the fast polarization switch, the phase is modulated with $\pm\pi/2$ at around



the current of 25 A. For example, at 700eV, based on the relationship in Fig. 20, the oscillation of $25 \pm \sim 0.59$ A is required to obtain the amplitude of $\pi/2$ or $\lambda/4$ at 25 A. The pattern of this AC current is shown in Fig. 21. By making the amplitude very small, the requirements on the switching power supply becomes relatively low. As shown in Fig. 22, it would be easy to understand that the phase of the LH and LV polarization is aligned without the phase modulation, and the polarization is set to 45° linear polarization. In this setting, the phase modulation of $\pm\pi/2$ continuously switches the polarization from 45° linear polarization to left and right CP via elliptical polarization. To set up the PMPSs and EMPSs in this way, first the current of EMPSs are set to the center value of the modulation. Then, PMPS1, PMPS3, PMPS5, and PMPS7 have to be set to generate 45° linear polarization in pairs of ID1-ID2, ID3-ID4, ID5-ID6, and ID7-ID8, and PMPS2, PMPS4, and PMPS6 are set to maximize the photon flux, resulting in 45° linear polarization by eight IDs. For the polarization switch, EMPS1, EMPS3, EMPS5, and EMPS7 oscillate the phase by $\pm\pi/2$. This results in the polarization modulation in each ID pair as shown in Fig. 22. At the same time, EMPS2, EMPS4, and EMPS6 should be modulated to keep $\varphi_1 + \varphi_2 = 2\pi$ by canceling the modulation by EMPS1, EMPS3, EMPS5, and EMPS7. "ID07" allows such polarization switch at up to 13 Hz. This continuous polarization modulation is the main feature of the polarization switch by the SCU.

Here, we will discuss the effect on the electron orbit and the light source position during the polarization switching in SCU. From the results of the off-line measurements



[29], the deviation angle during the switching was evaluated to be much smaller than the beam divergence, and no influence on the electron orbit was expected. After installing into the ring, the scheme of the orbital correction has been improved and the disturbance to closed orbit distortion is now under detection. On the other hand, in the case of the polarization switching for a twin-helical undulator combined with kickers, for example, ID25 in SPring-8 inevitably disturbs the COD by a few μm . Concerning the source position, in the SCU, it is the phase that the EMPS changes, and since the light source positions of the eight IDs do not change at all, the position of the light source obtained from those eight IDs does not change at all during the switching. This is in contrast to the switching with the kickers, where the polarization is changed by switching the IDs placed at different positions that produce different polarizations, so the position of the light source is generally shifted by the order of meter. Recently, a different approach for the faster polarization switching was proposed [37], but this also changes the light source position during the polarization switching. It should be emphasized that the advantage of the SCU is that the effect on the electron orbit is very small, almost negligible, and that the position of the light source does not change.

3 Examples of unique experiments

Synchrotron radiation has various advantages and offers highly brilliant, energy-tunable, and polarized X-ray. The beam has become indispensable probe for a wide variety of experiments and applications. Among a numerous number of the methods, developed at the synchrotron radiation facilities, X-ray absorption spectroscopy (XAS) is the most fundamental one in the soft X-ray region [5, 7]. An experiment of XAS is made by measuring amount of the light absorption of a sample typically at the absorption edges of the composing elements. The spectral data directly reflect electronic structure of a matter and the polarization dependence further reveals the microscopic picture, such orbitals and spins of the electronic state. XMCD is well known as a measurement using the polarization switching, and we have also demonstrated the power of the polarization switching of ID07 to detect the very weak XMCD signal. We have confirmed that XMCD

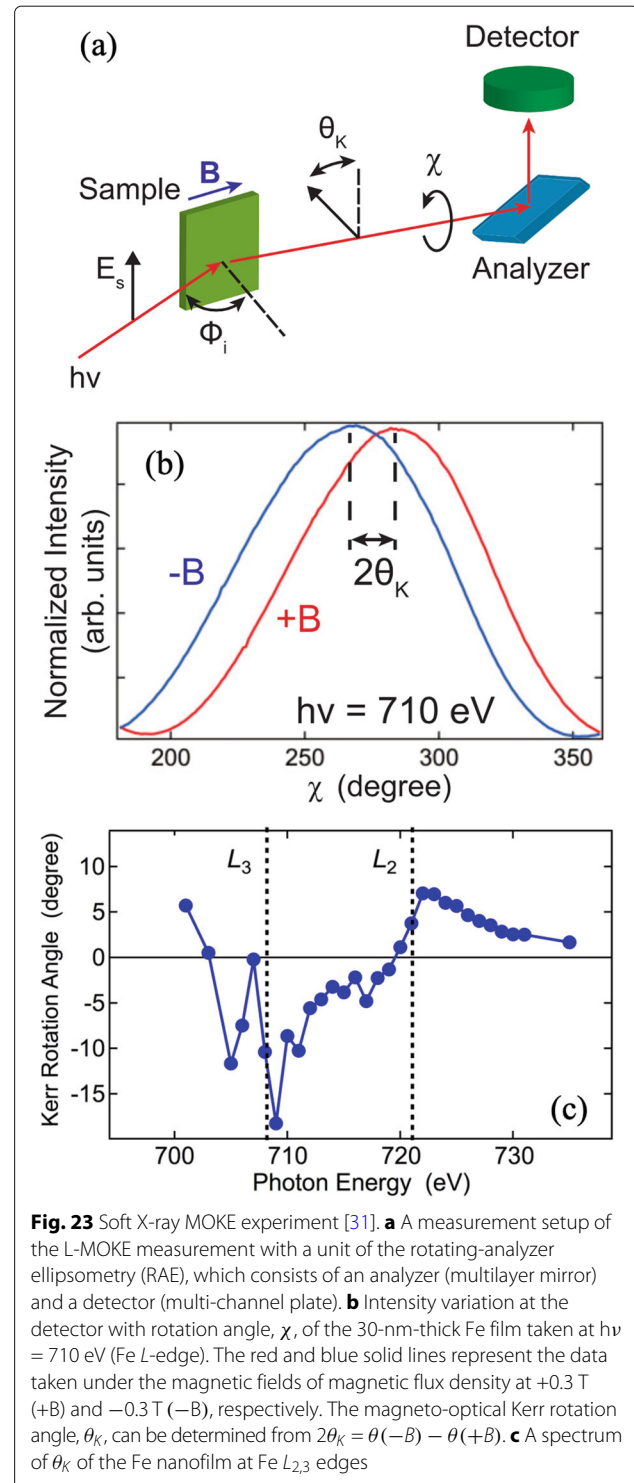
of $\sim 0.1\%$ XMCD signal, which could not be observed by the static measurement, can be observed by using polarization switching. In this section, we introduce examples of the XAS experiment with the unique polarization controls by SCU.

3.1 Soft X-ray magneto-optical spectroscopy

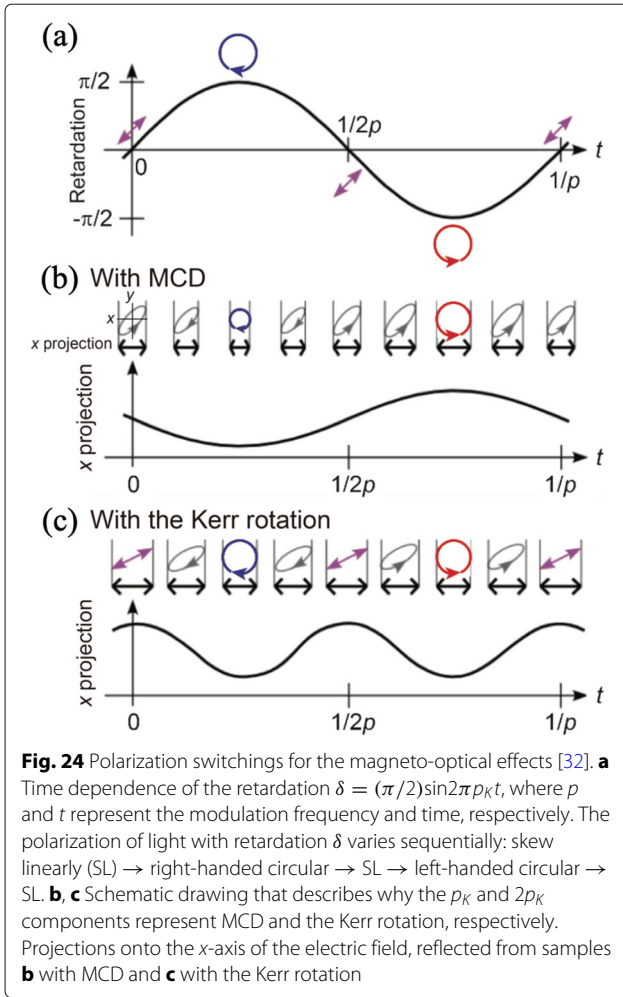
A well-known example of the polarization-dependent XAS experiment is a measurement of XMCD [5, 38–41]. XMCD data are obtained by difference of XAS spectra taken at opposite helicity of circularly polarized light at absorption edges of magnetic elements. On the other hand, irradiation of linearly polarized light on a magnetic sample results in magneto-optical Kerr or Faraday effect. The magneto-optical Kerr effect (MOKE) is resonantly enhanced when the probing photon energy is tuned at the absorption edge (X-ray MOKE, XMOKE) [31, 42]. These magneto-optical spectroscopies with soft X-ray provide magnetic information of a sample with element-selectivity. Polarization controlled undulator, such as APPLE-II, allows us to make such an experiment of XMCD or XMOKE. On the other hand, SCU is able to make simultaneous measurements of both XMCD and XMOKE that leads to quantitative determination of the element-specific complex permittivity. The experiment carried out by a combination of the fast polarization switching and a measurement geometry of MOKE. Thus, we begin the description by recalling experimental procedure of RMOKE of a magnetic sample.

Figure 23(a) presents the geometric setup for an experiment of longitudinal MOKE (L-MOKE), performed at SPring-8 BL07LSU [31]. A sample, the magnetic heterostructure of Ta/Cu/Fe/MgO, was illuminated by the s -polarized light at an incident angle (ϕ_i) of 80° with respect to the surface normal. A magnetic field was applied along the in-plane direction since the buried Fe nanofilm has an in-plane easy direction of magnetization. In MOKE, the reflected beam changes its polarization axis and the rotation angle corresponds to the magneto-optical Kerr rotation angle, θ_k . A measurement of θ_k is made by the rotating-analyzer ellipsometry (RAE). A unit of RAE rotates with χ around the beam axis and it is composed of an analyzer (multilayer mirror) and a detector (microchannel plate). Figure 23(b) plots variation of intensity at the detector with χ . The $2\theta_k$ value is determined from the angular difference in the ellipsometry curves taken at the opposite magnetic fields. As shown in Fig. 23(c), a spectrum of θ_k of the buried Fe nanofilm was taken at the Fe $L_{2,3}$ edges, resulting in negative (-18°) and positive (7°) values at the L_3 and L_2 absorption edges, respectively.

An SCU at SPring-8 BL07LSU is composed undulator segments of horizontally and vertically linearly polarized light. The SCU source is capable to make polarization



switching continuously [32]. Figure 24(a) shows a relation between the phase modulation ($-\pi/2 - \pi/2$) and the light polarization at a frequency of p_K . The phase retardation varies periodically by $\delta = (\frac{\pi}{2})\sin 2\pi p_K t$. The light polarization changes continuously from linear to right-



or left-handed circular. Using this polarization-modulated beam in magneto-optical experiments, the ellipticity (ϵ_K) appears in signals at the p_K frequency by the magnetic circular dichroism (MCD), while the Kerr rotation angle (θ_K) at the $2p_K$ frequency by the optical rotation. Consequently, XMCD (ϵ_K) and XMOKE (θ_K) are measurable simultaneously by extracting the p_K and $2p_K$ components in the reflection intensity.

At the RAE geometry of the s-polarized light configuration ($\chi = \pi/2$, Fig. 25(a)), intensities at the detector, $I(0)$, $I(p_K)$, and $I(2p_K)$, are described as follows:

$$I(0) = C_s \left[1 + \theta_K^{s2} + \epsilon_K^{s2} + 2\theta_K^s J_0(\pi/2) \right] \quad (17)$$

$$I(p_K) = 4C_s \epsilon_K^s J_1(\pi/2) \quad (18)$$

$$I(2p_K) = 4C_s \theta_K^s J_2(\pi/2) \quad (19)$$

where C_s is a constant for the s wave and $J_n(\pi/2)$ is the n th order Bessel function at $\pi/2$. In the p-polarized light configuration ($\chi = 0$, Fig. 25(b)), the intensities are given as:

$$I(0) = C_p \left[1 + \theta_K^{p2} + \epsilon_K^{p2} + 2\theta_K^p J_0(\pi/2) \right] \quad (20)$$

$$I(p_K) = 4C_p \epsilon_K^p J_1(\pi/2) \quad (21)$$

$$I(2p_K) = 4C_p \theta_K^p J_2(\pi/2) \quad (22)$$

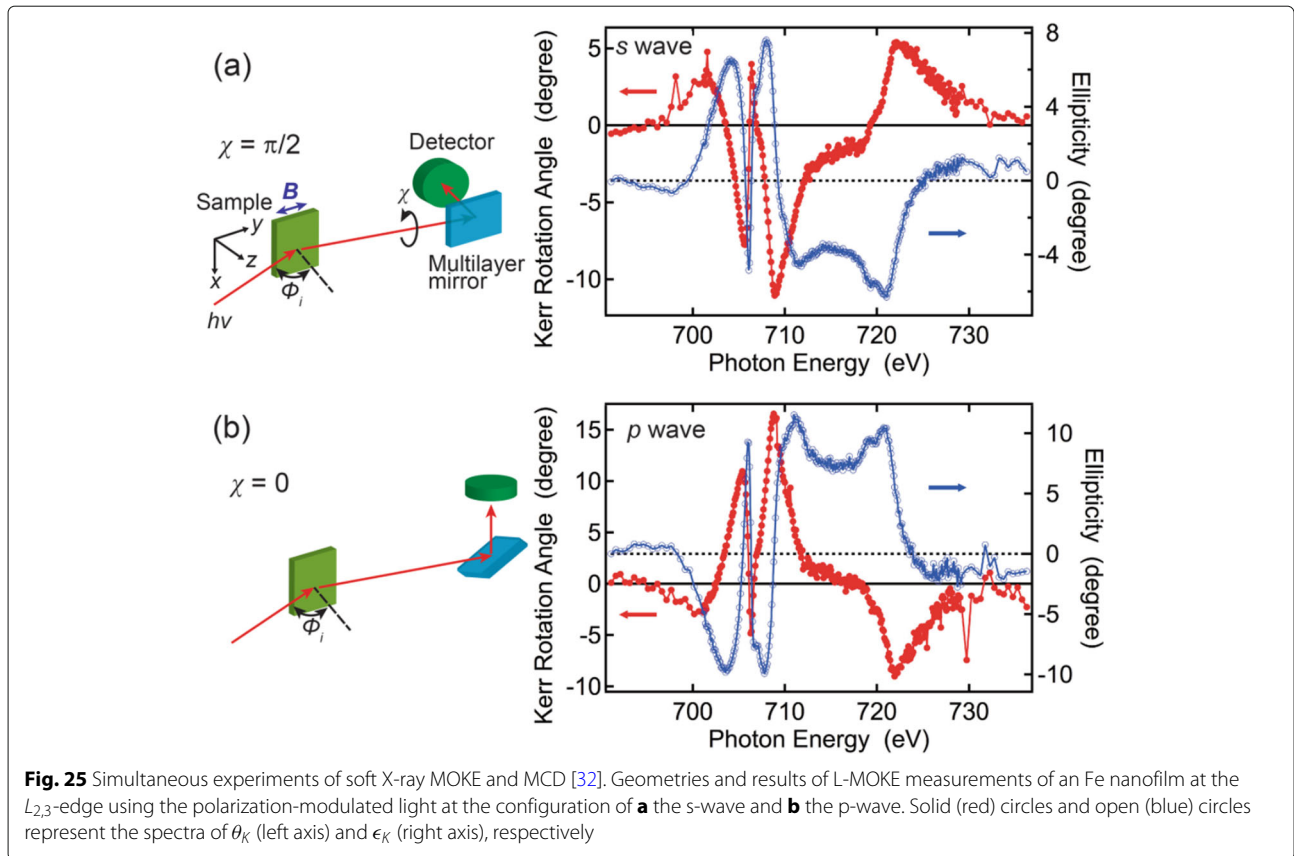
where C_p is a constant for the p wave. Details of the equations are described elsewhere [32].

Figure 25 summarizes results of the simultaneous measurement of θ_K and ϵ_K for the Fe nanofilm, obtained from $I(0)$, $I(p_K)$ and $I(2p_K)$ [32]. The ac current at the EMPS was set at 25 ± 0.588 A and frequency $p_K = 12.987$ Hz. A phase shift of $\pi/2$ corresponded to the current of 0.588 A. The spectra are inverted between s and p wave configuration. The θ_K spectra in Fig. 25 is consistent with the θ_K spectrum in Fig. 24. Thanks to the high-sensitive measurement by the lock-in detection by the frequency modulation, fine spectral features can be measured in the spectra in Fig. 25. The θ_K and ϵ_K spectra appear to be derivatives of each other, which is consistent with the relationship expressed by the Kramers-Kronig relations. One can compare results of Fig. 23(c) and Fig. 25 that were taken by the conventional/static measurement and by the switching experiments with the lock-in detection, respectively. The novel approach significantly reduces the measurement time, increases the datapoints, and improves the signal-to-noise ratio.

A combination of the θ_K and ϵ_K values benefits determination of the complex permittivity, ϵ_{xz} , of the Fe nanofilm [32], as shown in Fig. 26(a). The Kramers-Kronig relations is confirmed again between the real and the imaginary parts. For a comparison, the permittivity of bulk Fe (bcc) was calculated based on first-principles within the KKR formalism (Fig. 26(b)). One can find good agreement between the experimental and theoretical ϵ_{xz} spectra. The present method with the polarization control by SCU reliably outputs the off-diagonal component of permittivity in the SX region and the apparent reproduction from the first-principles calculation indicates that it is useful in evaluating the spin-polarized electronic structure of materials. Through a deep comparison, the dip in the Im curve and the peak in Re curve at the L_3 edge were additionally found in the experimental ϵ_{xz} spectra. The spectral feature is due to the interference effects and it further carries information non-uniform properties of a sample, such as nano-structures and interfaces [32].

3.2 Near-edge X-ray absorption fine structure

Among modern X-ray techniques, near-edge X-ray absorption fine structure (NEXAFS) has been recognized as a canonical tool to determine orbital configuration of materials [8]. From the intensity, width, and energy position of absorption peaks, one can obtain essential information about chemical bonds such as species, length, and orientation. Recent years have witnessed application



of NEXAFS to diverse systems, ranging from bulk crystals [43] to mono-layer sheets [44, 45] and chemisorbed atoms and molecules at a surface [46]. Being indispensable for condensed-matter physics/chemistry and surface science, NEXAFS has now been developed into a new direction to combine with nano-scale imaging and *operando* experiments [47–49], which will allow us, for example, to optimize functionalities of molecular nano-devices.

The cross section σ of X-ray absorption from a state $|i\rangle$ to $|f\rangle$, under the dipole approximation, is described by the Fermi's golden rule,

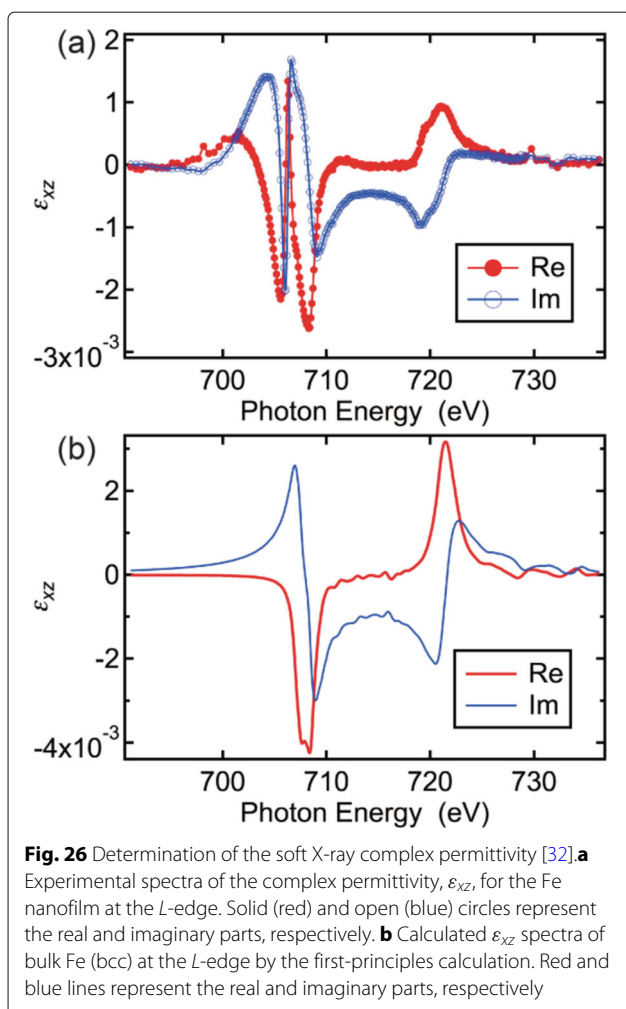
$$\sigma \propto \left| \langle f | \mathbf{E} \cdot \mathbf{p} | i \rangle \right|^2, \quad (23)$$

where \mathbf{E} is the electric-field vector and \mathbf{p} is the momentum operator of electrons [8]. Let us assume that the absorption occurs at the K-edge of light elements like C and N. In such cases, the above matrix element is reduced to a function of the angle between final-state $2p$ -orbital orientation and incident-light polarization [8]. One can therefore determine the orientation of unoccupied, anti-bonding orbitals by inspecting the angular profile of the absorption intensity either with rotating samples or light polarization. Due to the difficulty of rotating linear polarization, a conventional approach has been to change the sample polar angle as shown in Fig. 27(a). One shortcoming of this method is the deviation of beam spot due to

inevitable misalignment of the rotational center. Whereas uniform samples with reasonably large area are measurable, unreliability of the spot position hampers measurements of small-size crystals or nano-structured devices. Moreover, under *operando* condition, the movement of the sample itself is severely constrained. To meet a growing demand to study nano-structured functional devices in various conditions, therefore, the development of an alternative method is desired for carrying out NEXAFS measurements.

In this section, we describe the implementation of rotational linear polarization at SPring-8 BL07LSU by use of an SCU, which enables NEXAFS measurements while totally fixing the sample position and angle (Fig. 27(b)). Its operation principle and recent application to a NEXAFS measurement of hexagonal boron nitride (h-BN) are presented [33].

To demonstrate the feasibility of NEXAFS measurements using rotational linear polarization, we here present our recent NEXAFS study on h-BN [33], a typical two-dimensional material. Figure 28(a) and (b) display the results of conventional N K-edge NEXAFS measurement conducted at room temperature by varying sample polar angles (Fig. 27(a)). When horizontal polarization is used, the spectra obtained at grazing (80°) and normal incidence exhibit sharp contrast in the peak intensity at

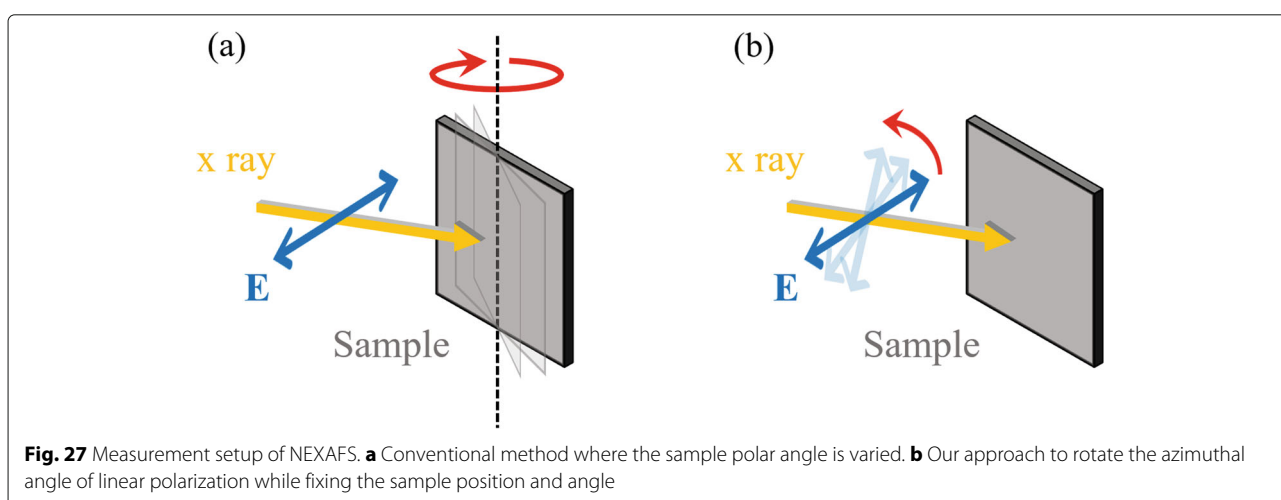


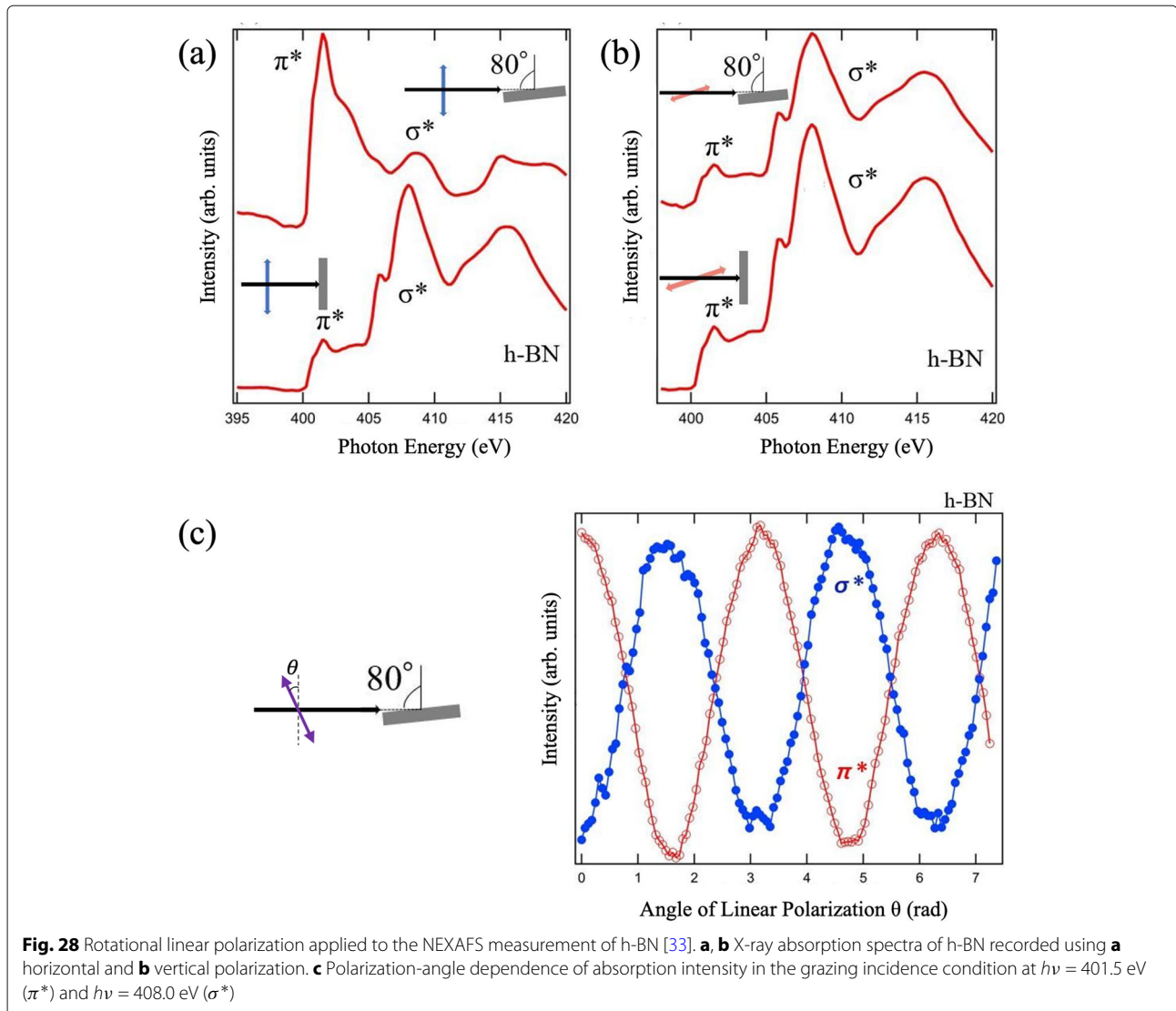
401.5 eV and 408.0 eV (Fig. 28(a)). From the matrix element in Equation 23, grazing (normal) incident light is supposed to promote electrons into the $2p \pi^*$ (σ^*) orbital, which is pointing out-of-plane (lying in-plane). We hence assign the peak at 401.5 (408.0) eV to the transition into

the π^* (σ^*) orbital. On the other hand, relative peak intensity does not depend significantly on the incident angle when vertical polarization is selected (Fig. 28(b)). This observation is in accord with the electric-field vector of the vertical polarization lying always in-plane.

Having acquired reasonable results from the conventional NEXAFS, polarization-rotation NEXAFS measurements (Fig. 27(b)) were attempted at fixed incident angle and photon energies. The red curve of Fig. 28(c) represents the absorption intensity at 401.5 eV (π^* orbital), measured with grazing incidence. In this geometry, azimuthal rotation of the polarization vector changes its in- and out-of-plane components with respect to the sample. The absorption intensity is thus expected to show a $\cos^2\theta$ dependence [8]. The intensity oscillation with a periodicity of π —observed in Fig. 28(c)—therefore assures that the polarization angle is under control as designed. Upon swapping left and right circular polarization, i.e., reversing the relative phase difference, the same occurs to the intensity maxima and minima [33]. This can be understood by considering the operation $\theta \rightarrow -\theta$ in Equations 15 and 16, which converts vertical polarization ($\theta + \pi/4 = \pi/2$) to horizontal one ($\theta + \pi/4 = 0$).

Turning to the absorption into the σ^* orbital (the blue curve in Fig. 28(c)), one finds intensity oscillation of the same periodicity but with the rotation angle shifted by $\pi/2$. This is in perfect agreement with the switch of the target orbital, from π^* to σ^* . At the normal incidence, the signal is virtually insensitive to the rotation of the polarization vector in all the conditions [33]. This result is again consistent with the fact that the polarization vector has an in-plane component only, irrespective of the polarization angle, in the normal-incidence condition. In summary, Fig. 28(c) shows the central results from the rotational NEXAFS measurement, highlighting clear contrast between σ^* and π^* orbitals. This kind of plot provides thorough information about the orbital orientation





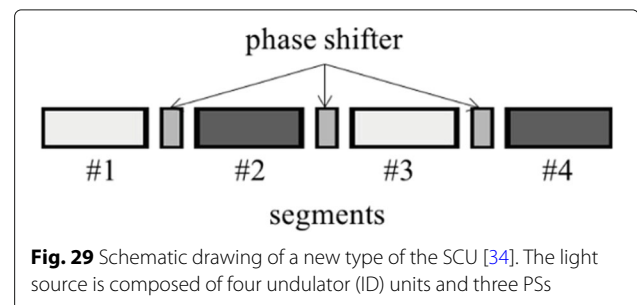
and hence will serve for determining precise electronic configuration of the sample.

4 Future outlook

4.1 Phase Interferometric Ensemble of APPLE-type undulator

A concept of an SCU can be extended to adopt the APPLE-II undulator as their segments. The detailed design and a simulation of the optical performance were reported by Matsuda et al. [34]. At an electron storage ring of the low-emittance ($\epsilon=1\text{nm}\cdot\text{rad}$) ring, the SCU can have total length of 4 m and it is composed of four undulator units and three PSs, as shown in Fig. 29. Compared to the SCU developed at SPring-8 BL07LSU, a segmented undulator of the Phase INterferometric Ensemble of APPLE (PINEAPPLE) undulator is much compact and generates soft X-rays with much varieties of the light polarization thanks to ID segments of the APPLE-II undulator.

As mentioned in the introduction, under the ideal conditions, the degree of the polarization is 100% even for the four-segmented undulator as shown in Fig. 3. However, in reality, the emittance value is practically so large that a degree of the polarization is consequently lower, as shown in Figs. 4 and 5. Thus, more segments are required in a typical synchrotron radiation ring. Therefore, the low



emittance ring is very desirable for the segmented undulator, where higher degree of polarization can be obtained with the fewer segmentation.

The flux and P_C for the same parameters as in [34] except for the emittance are shown in Fig. 30. The acceptance is $2\sigma \times 2\sigma$ of the side peak around 717 eV at each emittance. The larger the emittance, the larger the effect of the tail on the lower-energy side, and the degree of the polarization is severely deteriorated. Figure 31 shows the maximum P_C of the side peaks for different emittance and acceptance. As the emittance is reduced from 100 nmrad to 10 nmrad and from 10 nmrad to 1 nmrad, the degree of the polarization becomes much better, and at 1 nmrad, the degree of the polarization is almost close to the diffraction-limited value at 0.1 nmrad. Thus, the lower emittance is directly related to the improvement of the degree of the polarization, which shows the good compatibility with the segmented undulator for the next generation ring.

Figure 32 lists examples of polarized X-rays, produced by various combination of polarization modes in the APPLE units. In a configuration of an SCU, circular polarized light is generated with the horizontal linear undulators (#1 and #3) and the vertical linear undulators (#2 and #4). Since the individual segments simultaneously generate the intense higher-order beams of the linearly polarized light, higher order (e.g., third order) circular

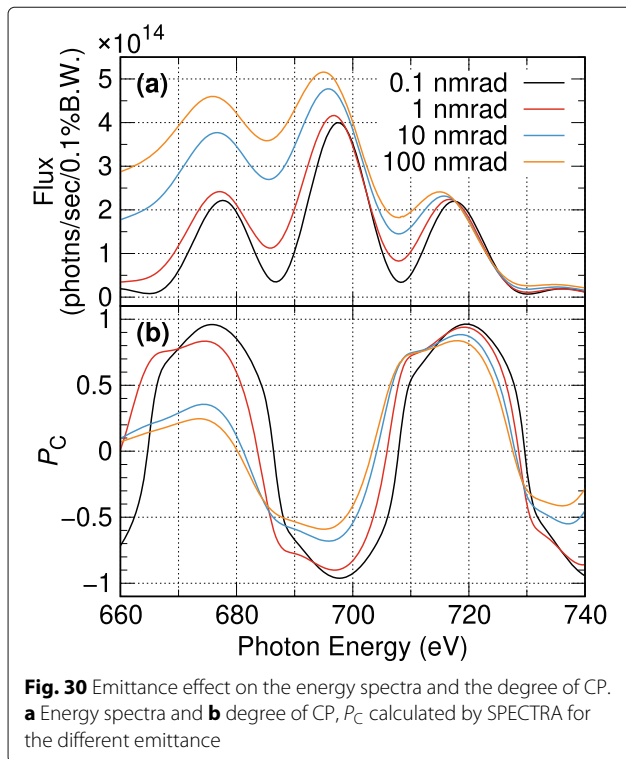


Fig. 30 Emittance effect on the energy spectra and the degree of CP. **a** Energy spectra and **b** degree of CP, P_C calculated by SPECTRA for the different emittance

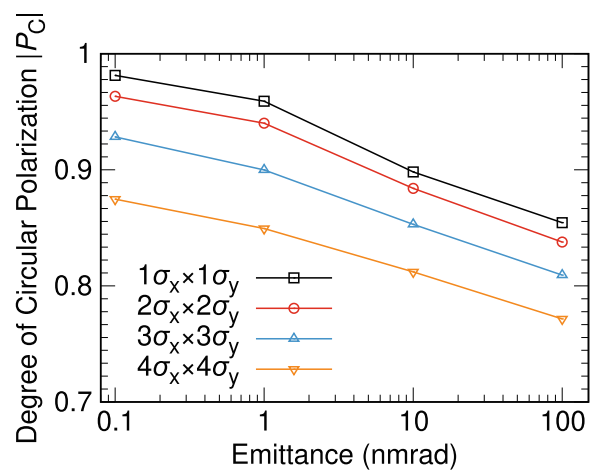


Fig. 31 The dependence of $|P_C|$ of the side peak on the emittance and acceptance

polarized light can be produced, extending available photon energy range for experiments at a beamline. This optical feature is sharply contrast to a conventional helical undulator that has limited to use only the photon energy range of the first order light. Adopting the PSs with electromagnetic coils, unique switching mode, described in the previous section, can be operated.

Linear polarized light is generated with the helical (+h) undulators (#1 and #3) and the opposite helical (-h) undulators (#2 and #4). Since the higher order beam from a helical undulator is negligible, the linearly polarized soft X-ray is intrinsically used only for the first order beam. This has an advantage of suppressing the high-order light and reducing the heat load at the on-axis beam that often becomes problems for a conventional linear undulator. A unique polarization mode of the angular rotation of the linear polarization can be operated as described in the previous section.

The segmented undulator with the APPLE units, of course, is flexible to take a configuration in which all the segments are the same type: for example, circular polarized light by four helical (+h) undulators (#1-#4) or linear polarized light by the four linear (horizontal) undulators (#1-#4). The optical performance is equivalent to a long undulator that is solely a helical or linear undulator.

Beside a list in Fig. 32, the APPLE undulator segment leaves a possibility of combining a different set of polarization modes. For example, a researcher can set one type of segment in helical mode and the other in linear mode. This configuration allows us to generate photon vortices and also to characterize the topologically polarized modes [50-53]. Higher harmonics, produced by a helical undulator, are known to have a singularity at the center of the beam and carry orbital angular momentum (OAM) that can be defined by the topological numbers. Recently, a

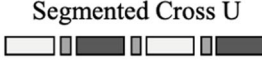
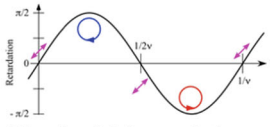
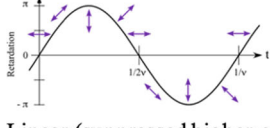


Undulator type	Polarization mode	Segment	
Segmented Cross U 	 Circular (higher-order)	#1 linear (horizontal) #2 linear (vertical) #3 linear (horizontal) #4 linear (vertical)	
	 Linear (suppressed higher-order)	#1 helical (+h) #2 helical (-h) #3 helical (+h) #4 helical (-h)	
	Segmented U 	Circular	#1 helical (+h) #2 helical (+h) #3 helical (+h) #4 helical (+h)
		Linear	#1 linear (horizontal) #2 linear (horizontal) #3 linear (horizontal) #4 linear (horizontal)
Long U 	Circular	helical (+h)	
	Linear	linear (horizontal)	

Fig. 32 A list of polarization examples that are prepared by combinations of polarization modes in the units of a segmented undulator (U) [34]. A single undulator (Long U) is shown for a reference

soft X-ray photon beam with OAM was observed in the second harmonic off-axis radiation of the helical undulator. Generation of the photon vortex was demonstrated by detecting a spiral pattern of photon intensity that is the result of interference between the second harmonic of the helical undulator and the fundamental light of the planar undulator. Therefore, the combination of helical and planar units within a segmented undulator can generate and, at the same time, characterize photon vortices for the beamline experiments, such as imaging of the topological samples [54].

4.2 Towards 1 kHz switching

The maximum frequency of the polarization switching at SPring-8 is currently 13 Hz, which is limited by an operation policy of the storage ring. As for the performance of the EMPs itself, we have already confirmed in off-line experiments that the disturbance to the electron trajectory should be small enough up to 50 Hz as shown in [29], and in principle, we believe that the polarization switching at this frequency can be realized soon. The reason why the frequency is limited to 13 Hz in the operation is to ensure the smooth commissioning and stable operation of the ring. In order to increase the frequency towards 1 kHz, it is necessary to prepare the powerful and accurate switch-

ing power supply and examine the effect of eddy current on the chamber. The faster the polarization switching, the larger the self-inductance, and the more power is required, indicating the more difficulty to achieve the accurate current control. These will require careful preparation and adjustment and may require a development. In addition, the performance of EMPs at fast switching will be confirmed at the off-line experiments, but it will be necessary to monitor whether the electron orbit is not really disturbed by the fast switching. This means that the sampling frequency of the electron beam position monitor should be higher than the switching frequency with enough accuracy. The fast switching such as 1 kHz can only be achieved through comprehensive development of the ring, not just ID, and we believe that continuous development is necessary for the faster polarization switching in the future.

4.3 Application in soft X-ray free electron laser

The present segmented undulators offer a promising application of polarization control for a soft X-ray free electron laser (SXFELs). The regulation has been a central issue in XFEL technology because there is no suitable polarizer at this photon energy region, which is in contrast to a case of the hard X-ray FEL [9]. Recently, there

has been reports of design and demonstration of polarization control by a cross undulator for soft X-ray FEL in the saturation regime at FERMI@ELETTRA [17–21]. The research has shown schemes for full and rapid control of X-ray polarization in a high-gain FEL. It is worth mentioning that a PS, controlled by EMPS, can be operated at 50 Hz. Since a SXFEL basically generates optical pulses at order of 10 Hz, e.g. 10–60 Hz, installation of the PS should make switching at any polarization mode at each SXFEL shot [29]. A combination of SXFEL with a cross or SCU will definitely provide much sophisticated and extensive experiment with the soft X-ray pulses.

4.4 Advanced experiments

This review article has shown that SCU allows us to change the soft X-ray beam at any polarization mode with fast-switching. An SCU has also advantage to keep a position of the light source during the polarization control. This important property of the light source makes the stable beam positioning at the beamline and the good compatibility with recent techniques of nano-focusing, spatial imaging, and spectromicroscopy [47–49]. Furthermore, the measurements can additionally be high-sensitive by combining with the lock-in amplification techniques by introducing the defined current into an electromagnetic coil in PS [29, 31]. Thus, a user station at the SCU beamline promisingly becomes a new platform for *operando* experiments to detect a faint dynamical change in a non-uniform functional material, such as catalysts, nanodevices, or biomaterials.

Acknowledgements

We gratefully acknowledge Shik Shin, Akito Kakizaki, and Masaharu Oshima for their guidance in constructing SPring-8 BL07LSU. We are grateful to Takashi Tanaka, Hideo Kitamura, Yasunori Senba, Haruhiko Ohashi, and Hiroaki Kimura for their collaborations on developing and in operating the undulator beamline. We thank Yuka Kosegawa and Mihoko Araki for their technical supports at the beamline. We wish to acknowledge Akane Agui and Masamitsu Takahashi for discussing future usages of the segmented undulator at a facility of the next-generation synchrotron radiation. We thank Naoka Nagamura for sharing her photos of the light source. The development was carried out as a research at the Synchrotron Radiation Research Organization, The University of Tokyo. Some of the experiments were made in the joint researches (Proposal No. 2021A7412, 2020A7411, 2019B7411, 2019B7410, 2019A7410, 2019A7411).

Authors' contributions

All the authors contributed developments, operations, and experiments of the undulator beamline.

Authors' information

Not applicable.

Funding

The research was carried out as a project of the Synchrotron Radiation Research Organization, The University of Tokyo. IM was partially supported by Grant-in-Aid for Scientific Research (KAKENHI 18H03874, 19H04398) from the Japan Society for the Promotion of Science (JSPS). JM was partially supported by Grant-in-Aid for Scientific Research (Kakenhi 18H03467) from JSPS.

Availability of data and materials

The data that support the findings of this study are available from the corresponding author, IM, upon reasonable request.

Declarations

Ethics approval and consent to participate

Not applicable.

Consent for publication

Not applicable.

Competing interests

The authors declare that they have no competing interests.

Author details

¹The Institute for Solid State Physics, The University of Tokyo, Kashiwa, Chiba 277-8581, Japan. ²National Institutes for Quantum Science and Technology, Sendai, Miyagi 980-8579, Japan.

Received: 31 March 2021 Accepted: 29 September 2021

Published online: 20 November 2021

References

1. J. A. Crowther, Röntgen Centenary and Fifty Years of X-Rays. *Nature*. **155**, 351 (1945). <https://doi.org/10.1038/155351a0>
2. P. C. Goodman, The new light: discovery and introduction of the X-ray. *Am. J. Roentgenol.* **165** (1995). <https://doi.org/10.2214/ajr.165.5.7572473>
3. N. Veasey, *X-Ray: seeing the Unseen*. (Wellbeck Publishing Group, London, 2014)
4. G. Margaritondo, *Introduction to synchrotron radiation*. (Oxford University Press, Oxford, 1988)
5. S. P. Cramer, *X-ray spectroscopy with synchrotron radiation*. (Springer, Berlin, 2020). <https://doi.org/10.1007/978-3-030-28551-7>
6. T. Tanaka, Current status and future perspectives of accelerator-based x-ray light sources. *J. Optics*. **19**, 093001 (2017). <https://doi.org/10.1088/2040-8986/aa7bf7>
7. J. A. Van Bokhoven, C. Lamberti (eds.), *X-ray absorption and X-ray emission spectroscopy: theory and applications* (John Wiley & Sons, New York, 2016)
8. J. Stöhr, *NEXAFS spectroscopy*. (Springer, Berlin, 2003)
9. M. Suzuki, Y. Inubushi, M. Yabashi, T. Ishikawa, Polarization control of an X-ray free-electron laser with a diamond phase retarder. *J. Synchrotron Radiat.* **21**, 466 (2014). <https://doi.org/10.1107/S1600577514004780>
10. S. Sasaki, K. Kakuno, T. Takada, T. Shimada, K. Yanagida, Y. Miyahara, Design of a new type of planar undulator for generating variably polarized radiation. *Nucl. Instrum. Meth. Phys. Res. A*. **331**, 763 (1993). [https://doi.org/10.1016/0168-9002\(93\)90153-9](https://doi.org/10.1016/0168-9002(93)90153-9)
11. S. Sasaki, Analyses for a planar variably-polarizing undulator. *Nucl. Instrum. Meth. Phys. Res. A*. **347**, 83 (1994). [https://doi.org/10.1016/0168-9002\(94\)91859-7](https://doi.org/10.1016/0168-9002(94)91859-7)
12. K. J. Kim, A synchrotron radiation source with arbitrarily adjustable elliptical polarization. *Nucl. Inst. Methods Phys. Res. A*. **219**, 425 (1984). [https://doi.org/10.1016/0167-5087\(84\)90354-5](https://doi.org/10.1016/0167-5087(84)90354-5)
13. S. Sasaki, R. Schlueter, S. Marks. Crossed elliptical polarization undulator (EEE, 1998). <https://epaper.kek.jp/pac97/papers/pdf/6V015.PDF>
14. J. Bahrd, et al., Circularly polarized synchrotron radiation from the crossed undulator at BESSY. *Rev. Sci. Instrum.* **63**, 339 (1992). <https://doi.org/10.1063/1.1142750>
15. T. Kaneyasu, Y. Hikosaka, M. Fujimoto, H. Iwayama, M. Katoh, Polarization control in a crossed undulator without a monochromator. *New J. Phys.* **22**, 083062 (2020). <https://doi.org/10.1088/1367-2630/aba730>
16. T.-Y. Chung, C.-S. Yang, Y.-L. Chu, F.-Y. Lin, J.-C. Jan, C.-S. Hwang, Investigating excitation-dependent and fringe-field effects of electromagnet and permanent-magnet phase shifters for a crossed undulator. *Nucl. Inst. Methods Phys. Res. A*. **850**, 72 (2017). <https://doi.org/10.1016/j.nima.2017.01.011>
17. E. Ferrari, E. Roussel, J. Buck, C. Callegari, R. Cucini, G. D. Ninno, B. Diviacco, D. Gauthier, L. Giannessi, L. Glaser, G. Hartmann, G. Penco, F. Scholz, J. Seltmann, I. Shevchuk, J. Viehhaus, M. Zangrando, E. M. Allaria1, Free electron laser polarization control with interfering crossed polarized fields. *Phys. Rev. Accel. Beams*. **22**, 080701 (2019). <https://doi.org/10.1103/PhysRevAccelBeams.22.080701>
18. E. Ferrari, E. Allaria, J. Buck, et al., Single Shot Polarization Characterization of XUV FEL Pulses from Crossed Polarized Undulators. *Sci Rep.* **5**, 13531 (2015). <https://doi.org/10.1038/srep13531>

19. Y. Ding, Z. Huang, Statistical analysis of crossed undulator for polarization control in a self-amplified spontaneous emission free electron laser. *Phys. Rev. Spec. Top. Accel. Beams*. **11**, 030702 (2008). <https://doi.org/10.1103/PhysRevSTAB.11.030702>
20. H. Deng, et al., Polarization switching demonstration using crossed-planar undulators in a seeded free-electron laser. *Phys. Rev. Spec. Top. Accel. Beams*. **17**, 020704 (2014). <https://doi.org/10.1103/PhysRevSTAB.17.020704>
21. H. Geng, Y. Ding, Z. Huang, Crossed undulator polarization control for X-ray FELs in the saturation regime. *Nucl. Instrum Methods Phys. Res. A*. **622**, 276 (2010). <https://doi.org/10.1016/j.nima.2010.07.050>
22. K.-J. Kim, Circular polarization with crossed-planar undulators in high-gain FELs. *Nucl. Instr. Methods Phys. Res. A*. **445**, 329 (2000). [https://doi.org/10.1016/S0168-9002\(00\)0137-6](https://doi.org/10.1016/S0168-9002(00)0137-6)
23. Y. K. Wu, N. A. Vinokurov, S. Mikhailov, J. Li, V. Popov, High-Gain Lasing and Polarization Switch with a Distributed Optical-Klystron Free-Electron Laser. *Phys. Rev. Lett.* **96**, 224801 (2006). <https://doi.org/10.1103/PhysRevLett.96.224801>
24. T. Tanaka, H. Kitamura, Simple scheme for harmonic suppression by undulator segmentation. *J. Synchrotron Radiat.* **9**, 266 (2002). <https://doi.org/10.1107/S0909049502005472>
25. T. Tanaka, H. Kitamura, Production of linear polarization by segmentation of helical undulator. *Nucl. Instrum. Methods*. **490**, 583 (2002). [https://doi.org/10.1016/S0168-9002\(02\)01094-X](https://doi.org/10.1016/S0168-9002(02)01094-X)
26. T. Tanaka, H. Kitamura, Improvement of Crossed Undulator for Higher Degree of Polarization. *AIP Conf. Proc.* **705**, 231 (2004). <https://doi.org/10.1063/1.1757776>
27. S. Yamamoto, Y. Senba, T. Tanaka, H. Ohashi, T. Hirono, H. Kimura, M. Fujisawa, J. Miyawaki, A. Harasawa, T. Seike, S. Takahashi, N. Nariyama, T. Matsushita, M. Takeuchi, T. Ohata, Y. Furukawa, K. Takeshita, S. Goto, Y. Harada, S. Shin, H. Kitamura, A. Kakizaki, M. Oshima, I. Matsuda, New soft X-ray beamline BL07LSU at SPring-8. *J. Synchrotron Radiat.* **21**, 352 (2014). <https://doi.org/10.1107/S1600577513034796>
28. Y. Senba, S. Yamamoto, H. Ohashi, I. Matsuda, M. Fujisawa, A. Harasawa, T. Okuda, S. Takahashi, N. Nariyama, T. Matsushita, T. Ohata, Y. Furukawa, T. Tanaka, K. Takeshita, S. Goto, H. Kitamura, A. Kakizaki, M. Oshima, New soft X-ray beamline BL07LSU for long undulator of SPring-8: Design and status. *Nucl. Instr. Meth. Phys. Res. A*. **649**, 58 (2011). <https://doi.org/10.1016/j.nima.2010.12.242>
29. I. Matsuda, A. Kuroda, J. Miyawaki, Y. Kosegawa, S. Yamamoto, T. Seike, T. Bizen, Y. Harada, T. Tanaka, H. Kitamura, Development of an electromagnetic phase shifter using a pair of cut-core coils for a cross undulator. *Nucl. Instrum. Meth. Phys. Res. A*. **767**, 296 (2014). <https://doi.org/10.1016/j.nima.2014.08.037>
30. T. Tanaka, H. Kitamura, Figure-8 undulator as an insertion device with linear polarization and low on-axis power density. *Nucl. Instr. Methods Phys. Res. A*. **364**, 368 (1995). [https://doi.org/10.1016/0168-9002\(95\)00462-9](https://doi.org/10.1016/0168-9002(95)00462-9)
31. Y. Kubota, Y. Hirata, J. Miyawaki, S. Yamamoto, H. Akai, R. Hobar, S. Yamamoto, K. Yamamoto, T. Someya, K. Takubo, Y. Yokoyama, M. Araki, M. Taguchi, Y. Harada, H. Wadati, M. Tsunoda, R. Kinjo, A. Kagamihata, T. Seike, M. Takeuchi, T. Tanaka, S. Shin, I. Matsuda, Determination of the element-specific complex permittivity using a soft x-ray phase modulator. *Phys. Rev. B*. **96**, 214417 (2017). <https://doi.org/10.1103/PhysRevB.96.214417>
32. Y. Kubota, M. Taguchi, H. Akai, S. Yamamoto, T. Someya, Y. Hirata, K. Takubo, M. Araki, M. Fujisawa, K. Yamamoto, Y. Yokoyama, S. Yamamoto, M. Tsunoda, H. Wadati, S. Shin, I. Matsuda, *L*-edge resonant magneto-optical Kerr effect of a buried Fe nanofilm. *Phys. Rev. B*. **96**, 134432 (2017). <https://doi.org/10.1103/PhysRevB.96.134432>
33. Y. Kudo, Y. Hirata, M. Horio, M. Niibe, I. Matsuda, A novel measurement approach for near-edge x-ray absorption fine structure: Continuous 2π angular rotation of linear polarization. *Nucl. Instrum. Methods*. **1018**, 165804 (2021). <https://doi.org/10.1016/j.nima.2021.165804>
34. I. Matsuda, S. Yamamoto, J. Miyawaki, T. Abukawa, T. Tanaka, Segmented Undulator for Extensive Polarization Controls in ≤ 1 nm-rad Emittance Rings. *e-J. Surf. Sci. Nanotechnol.* **17**, 41 (2019). <https://doi.org/10.1380/ejssnt.2019.41>
35. M. Born, E. Wolf, *Principle of optics*. (Pergamon, Oxford, U.K., 1975)
36. T. Tanaka, H. Kitamura, *SPECTRA*: a synchrotron radiation calculation code. *J. Synchrotron Radiat.* **8**, 1221 (2001). <https://doi.org/10.1107/S090904950101425X>
37. K. Hollmack, C. Schüssler-Langeheine, P. Goslawski, N. Pontius Kachel, F. Armbrorst, M. Ries, A. Schällicke, M. Scheer, W. Frentrup, J. Bahrtdt, Flipping the helicity of X-rays from an undulator at unprecedented speed. *Commun Phys.* **3**, 61 (2020). <https://doi.org/10.1038/s42005-020-0331-5>
38. C. T. Chen, Y. U. Idzerda, H.-J. Lin, N. V. Smith, G. Meigs, E. Chaban, G. H. Ho, E. Pellegrin, F. Sette, Experimental Confirmation of the X-Ray Magnetic Circular Dichroism Sum Rules for Iron and Cobalt. *Phys. Rev. Lett.* **75**, 152 (1995). <https://doi.org/10.1103/PhysRevLett.75.152>
39. Y. Kubota, K. Murata, J. Miyawaki, K. Ozawa, M. Onbasli, T. Shirasawa, B. Feng, S. Yamamoto, R.-Y. Liu, S. Yamamoto, S. Mahatha, P. Sheverdyayeva, P. Moras, C. Ross, S. Suga, Y. Harada, K. Wang, I. Matsuda, Interface electronic structure at the topological insulator/ferromagnetic insulator junction. *J. Phys. Condens. Matter*. **29**, 055002 (2017). <https://doi.org/10.1088/1361-648X/29/5/055002>
40. M. Suzuki, N. Kawamura, M. Mizukami, A. Urata, H. Maruyama, S. Goto, T. Ishikawa, Helicity-Modulation Technique Using Diffractive Phase Retarder for Measurements of X-ray Magnetic Circular Dichroism. *J. Appl. Phys.* **37**, L1488 (1998). <https://doi.org/10.1143/jjap.37.L1488>
41. T. Muro, T. Nakamura, T. Matsushita, H. Kimura, T. Nakatani, T. Hirono, T. Kudo, K. Kobayashi, Y. Saitoh, M. Takeuchi, T. Hara, K. Shirasawa, H. Kitamura, Circular dichroism measurement of soft X-ray absorption using helicity modulation of helical undulator radiation. *J. Electron Spectrosc. Relat. Phenom.* **144–147**, 1101 (2005). <https://doi.org/10.1016/j.jelspec.2005.01.140>
42. M. F. Tesch, M. C. Gilbert, H.-C. Mertins, D. E. Bürgler, U. Berges, C. M. Schneider, X-ray magneto-optical polarization spectroscopy: an analysis from the visible region to the x-ray regime. *Appl. Opt.* **52**, 4294 (2013). <https://doi.org/10.1364/AO.52.004294>
43. M. Niibe, N. Takehira, T. Tokushima, Electronic Structure of Boron Doped HOPG: Selective Observation of Carbon and Trace Doped Boron by Means of X-ray Emission and Absorption Spectroscopy. *e-J. Surf. Sci. Nanotechnol.* **16**, 122 (2018). <https://doi.org/10.1380/ejssnt.2018.122>
44. I. Tateishi, N. T. Cuong, C. A. S. Moura, M. Cameau, R. Ishibiki, A. Fujino, S. Okada, A. Yamamoto, M. Araki, S. Ito, S. Yamamoto, M. Niibe, T. Tokushima, D. E. Weibel, T. Kondo, M. Ogata, I. Matsuda, Semimetallicity of free-standing hydrogenated monolayer boron from MgB₂. *Phys. Rev. Mater.* **3**, 024004 (2019). <https://doi.org/10.1103/PhysRevMaterials.3.024004>
45. W. Auwärter, Hexagonal boron nitride monolayers on metal supports: Versatile templates for atoms, molecules and nanostructures. *Surf. Sci. Rep.* **74**, 1 (2019). <https://doi.org/10.1016/j.surfrep.2018.10.001>
46. S. Yamamoto, H. S. Kato, A. Ueda, S. Yoshimoto, Y. Hirata, J. Miyawaki, K. Yamamoto, Y. Harada, H. Wadati, H. Mori, J. Yoshinobu, I. Matsuda, Direct Evidence of Interfacial Hydrogen Bonding in Proton-Electron Concerted 2D Organic Bilayer on Au Substrate. *e-J. Surf. Sci. Nanotechnol.* **17**, 49 (2019). <https://doi.org/10.1380/ejssnt.2019.49>
47. H. Fukidome, M. Kotsugi, K. Nagashio, et al., Orbital-specific Tunability of Many-Body Effects in Bilayer Graphene by Gate Bias and Metal Contact. *Sci Rep.* **4**, 3713 (2014). <https://doi.org/10.1038/srep03713>
48. M. Zajac, T. Giela, K. Freindl, K. Kollbek, J. Korecki, E. Madej, K. Pitala, A. Koziol-Rachwal, M. Sikora, N. Spiridis, J. Stepien, A. Szkudlarek, M. Slezak, T. Slezak, D. Wilgocka-Slezak, The first experimental results from the 04BM (PEEM/XAS) beamline at Solaris. *Nucl. Instr. Methods Phys. Res. B*. **492**, 43 (2021). <https://doi.org/10.1016/j.nimb.2020.12.024>
49. B. Watts, H. Ade, NEXAFS imaging of synthetic organic materials. *Mater. Today*. **15**, 148 (2012). [https://doi.org/10.1016/S1369-7021\(12\)70068-8](https://doi.org/10.1016/S1369-7021(12)70068-8)
50. J. Bahrtdt, K. Hollmack, P. Kuske, R. Müller, M. Scheer, P. Schmid, First Observation of Photons Carrying Orbital Angular Momentum in Undulator Radiation. *Phys. Rev. Lett.* **111**, 034801 (2013). <https://doi.org/10.1103/PhysRevLett.111.034801>
51. M. van Veenendaal, I. McNulty, Prediction of Strong Dichroism Induced by X Rays Carrying Orbital Momentum. *Phys. Rev. Lett.* **98**, 157401 (2007). <https://doi.org/10.1103/PhysRevLett.98.157401>
52. E. Hemsing, M. Dunning, C. Hast, T. Raubenheimer, D. Xiang, First Characterization of Coherent Optical Vortices from Harmonic Undulator Radiation. *Phys. Rev. Lett.* **113**, 134803 (2014). <https://doi.org/10.1103/PhysRevLett.113.134803>

53. M. Katoh, M. Fujimoto, N. S. Mirian, T. Konomi, Y. Taira, T. Kaneyasu, M. Hosaka, N. Yamamoto, A. Mochihashi, Y. Ta-kashima, K. Kuroda, A. Miyamoto, K. Miyamoto, S. Sasaki, Helical Phase Structure of Radiation from an Electron in Circular Motion. *Sci. Rep.* **7**, 6130 (2017). <https://doi.org/10.1038/s41598-017-06442-2>
54. Y. Ishii, K. Yamamoto, Y. Yokoyama, M. Mizumaki, H. Nakao, T. Arima, Y. Yamasaki, Soft-X-Ray Vortex Beam Detected by Inline Holography. *Phys. Rev. Appl.* **14**, 064069 (2020). <https://doi.org/10.1103/PhysRevApplied.14.064069>

Publisher's Note

Springer Nature remains neutral with regard to jurisdictional claims in published maps and institutional affiliations.